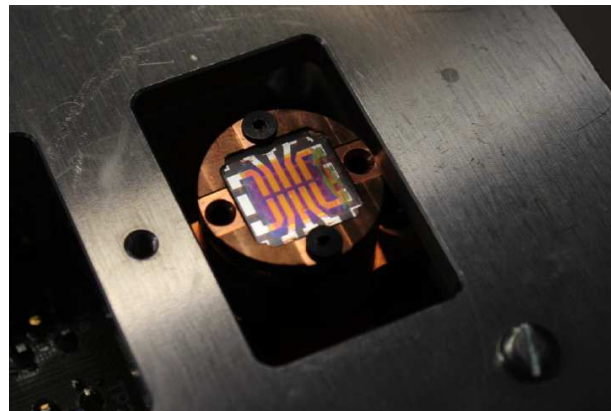


Spring Semester 2012

Prof. Dr. Vanessa Wood

Master Thesis

# Deep-Level Transient Spectroscopy on Solar Cells Based on Colloidal Nanocrystals



---

*Author:*

Michael Jakob

*Advisors:*Deniz Bozyigit  
Vanessa Wood



# Deep-Level Transient Spectroscopy on Solar Cells Based on Colloidal Nanocrystals

Michael Jakob

Advisors  
Deniz Bozyigit  
Vanessa Wood

September 30, 2012



Ich erkläre mit meiner Unterschrift, das Merkblatt Plagiat zur Kenntnis genommen, die vorliegende Arbeit selbständig verfasst und die im betroffenen Fachgebiet üblichen Zitievorschriften eingehalten zu haben.

Merkblatt Plagiat:

[http://www.ethz.ch/students/seminar/plagiarism\\_s\\_de.pdf](http://www.ethz.ch/students/seminar/plagiarism_s_de.pdf)

---

Ort, Datum

---

Unterschrift



# Acknowledgement

I would like to thank Prof. Dr. Vanessa Wood, head of the Laboratory for Nanoelectronics, for the opportunity to carry out my master thesis in her group and also for the excellent advices and inputs.

I am also thankful to Deniz Bozyigit, PhD student at the Laboratory for Nanoelectronics and my supervisor for this thesis, for his competent support and inspiration, without this work and the results would not have been possible.

I would like to thank Teut  Bunjaku, Val Miko  and Ouwen Xu for the help with the solar cell fabrication in the laboratory and the development of the IV measurement setup together with Deniz.

I would like to express my gratitude to my friends, especially to Matthias F ssler and Lukas Bruderer for the great support and answering to my complex questions.

Furthermore, I would like to thank the whole group at the Laboratory for Nanoelectronics for the help in the laboratory, the advices in the absence of my supervisor and also for the nice atmosphere I encountered during the thesis.

Last but not least, I would like to express my gratitude to my family, especially to my parents, Heinz and Doris Jakob, and my sister, Petra Jakob, for their great moral support.



# Abstract

Solar cells based on colloidal quantum dots (cQDs) are promising candidates for low-cost and high efficiency photovoltaics. cQDs enable solution-phase continuous coating processes and facile tuning of the bandgap via the change of their diameter to match the sun's broad visible- and infrared-containing spectrum.

Despite these great features, the cQDs used in photovoltaic devices are not yet well characterized. This thesis presents the first demonstration of deep-level transient spectroscopy (DLTS), which is a commonly used technique for studying defects in silicon solar cells, for the observation and analysis of deep-level traps in cQD solar cells. These trap states are believed to influence the electrical properties of the nanocrystal (NC) material and the device parameters.

Our solar cells under investigation consist of PbS cQDs assembled into a NC active layer, which was fabricated by layer-by-layer dip and spin coating processes. Our solar cells yielded a power conversion efficiency of 2.46% under AM1.5G conditions, which is comparable to literature values.

To investigate deep traps, a DLTS setup was developed with the possibility to measure current and capacitance transients.

Current transients were successfully acquired in three experiments, confirming that DLTS measurements can be performed on PbS solar cells. The transients were observed in a temperature range from 250 K to 340 K. From four different DLTS approaches, activation energies around 0.3 eV were extracted. Additionally, a trap density of  $2.5 \cdot 10^{16} \text{ cm}^{-3}$  was obtained, which is in good agreement with a Mott-Schottky analysis performed on the solar cells.

This thesis indicates the potential for DLTS measurements for understanding transport phenomena in cQD-based solar cells.



# Contents

<b>Abstract</b>	<b>i</b>
<b>1 Introduction to Colloidal Quantum Dot Solar Cells</b>	<b>1</b>
1.1 Third Generation Solar Cells . . . . .	1
1.2 PbS Schottky Solar Cells . . . . .	2
1.3 Motivation for Trap Investigation . . . . .	2
1.4 Thesis Outline . . . . .	2
<b>2 Review of Techniques for Electronic Trap State Investigation</b>	<b>3</b>
<b>3 Theory of Deep-Level States in Semiconductor Materials</b>	<b>5</b>
3.1 Defects . . . . .	5
3.2 Deep-Level Traps . . . . .	6
3.3 Shockley-Reed-Hall Theory . . . . .	6
3.4 Space Charge Spectroscopy . . . . .	8
3.4.1 Capacitance Measurement . . . . .	8
3.4.2 Current Measurement . . . . .	9
3.4.3 Temperature Effect on Capacitance and Current Measurements . . . . .	9
3.5 Deep-Level Transient Spectroscopy (DLTS) . . . . .	10
3.5.1 Conventional Boxcar DLTS . . . . .	10
3.5.2 Other DLTS Methods . . . . .	11
<b>4 Device Fabrication and Characterization</b>	<b>13</b>
4.1 Sample Preparation . . . . .	13
4.1.1 Materials . . . . .	13
4.1.2 Preparation Procedure . . . . .	14
4.1.3 Remarks and Conclusions . . . . .	18
4.2 Characterization of PbS Solar Cells . . . . .	20
4.2.1 Measurement Setup . . . . .	20
4.2.2 IV and CV Measurements . . . . .	21
4.2.3 Degradation Measurements in Dark . . . . .	23
4.2.4 Degradation Measurements in Light . . . . .	25
4.2.5 Impedance Spectroscopy . . . . .	25
4.2.6 Mott-Schottky Analysis . . . . .	26
4.2.7 Summary and Conclusions . . . . .	27

<b>5 Development of a Setup for DLTS Measurements on QD Solar Cells</b>	<b>29</b>
5.1 Capacitance vs. Current DLTS . . . . .	29
5.2 Hardware Configuration of the Setup . . . . .	29
5.3 Software of the Setup . . . . .	32
5.3.1 Software for Data Acquisition . . . . .	32
5.3.2 Software for Data Processing . . . . .	36
5.4 Characterization of the Setup . . . . .	38
5.4.1 Current Measurements with Transimpedance Amplifier (TIA) . . . . .	38
5.4.2 Noise Reduction Considerations . . . . .	39
5.4.3 Temperature Sensor Calibration . . . . .	39
<b>6 Current Transient DLTS on PbS Solar Cells</b>	<b>41</b>
6.1 First Transients Measurements - Prove of Concept . . . . .	41
6.2 DLTS Analysis on Measured Current Transients . . . . .	42
6.2.1 Description of the Experiment . . . . .	42
6.2.2 Boxcar Approaches . . . . .	43
6.2.3 Fourier and Direct Fitting Approach . . . . .	45
6.2.4 Carrier Trap Density . . . . .	46
6.3 Temperature Dependent IV Curves and Concurrent DLTS Measurement . . . . .	47
6.3.1 Description of the Experiment . . . . .	47
6.3.2 DLTS Measurements . . . . .	48
6.3.3 Temperature Dependent IV Measurements . . . . .	50
6.3.4 Saturation Current Model Fitting . . . . .	51
6.3.5 Summary and Conclusions . . . . .	53
<b>7 Summary and Conclusion</b>	<b>55</b>
<b>8 Outlook</b>	<b>57</b>
<b>Bibliography</b>	<b>59</b>
<b>A Database of Colloidal Solar Cells Fabricated for This Thesis</b>	<b>65</b>
<b>B Dip Coater</b>	<b>69</b>
<b>C Devices and Capacitance DLTS Setup</b>	<b>71</b>
C.1 Laboratory Devices . . . . .	71
C.2 Capacitance and Current DLTS Setup . . . . .	75
<b>D LabVIEW Features</b>	<b>77</b>
D.1 Temperature and Voltage Sweep . . . . .	77
D.2 Additional LabVIEW Settings . . . . .	78
<b>E Saturation Current Models</b>	<b>79</b>

# List of Figures

3.1	Band diagram for ideal and real semiconductor	5
3.2	Fundamental trap processes	6
3.3	Transient measurement protocol	8
3.4	Scheme of conventional Boxcar method	11
4.1	Structure of the produced samples	14
4.2	Dip coating procedure	15
4.3	Spin coating procedure	16
4.4	Spin coating set up with spin coater and solutions.	17
4.5	Finished colloidal PbS films	18
4.6	Three samples with partially detached films	18
4.7	IV measurement setup scheme	20
4.8	Dark and light IV characteristics	22
4.9	CV characteristics	23
4.10	Degradation measurements under dark conditions	24
4.11	Degradation measurements under illumination conditions	25
4.12	Impedance spectroscopy	26
4.13	Mott-schottky analysis	27
5.1	Current DLTS setup in the laboratory	30
5.2	Current DLTS setup schematic	31
5.3	Timing diagrams of single transient operation mode	33
5.4	LabVIEW single transient interface.	34
5.5	Timing diagrams of temperature setting	35
5.6	LabVIEW single temperature interface.	35
5.7	Data flow graph of data processing	37
5.8	IV test with transimpedance amplifier	39
5.9	Cryostat with attached sensor on samples surface.	40
6.1	Several investigations in a DLTS experiment	42
6.2	Measured current transients	43
6.3	Results of conventional Boxcar approach.	44
6.4	Results of Gaussian Boxcar approach.	45
6.5	Results of Fourier and direct fitting approach.	46
6.6	Carrier densities from DLTS measurement	47
6.7	Temperature dependent current transients	48
6.8	Baseline restored transients with Boxcar spectra	49
6.9	Fourier DLTS for second experiment	49

6.10 Temperature dependent IV characteristics . . . . .	50
6.11 IV curve model fitting . . . . .	52
B.1 Dip coater . . . . .	70
C.1 Agilent 33522 Arbitrary Waveform Generator (AWG) . . . . .	71
C.2 Janis ST-500 cryostat . . . . .	72
C.3 LakeShore 335 temperature controller. . . . .	72
C.4 Boonton 72ad capacitance meter . . . . .	73
C.5 Femto DHCPA transimpedance current amplifier. . . . .	74
C.6 Rohde and Schwartz RTM1054 oscilloscope . . . . .	74
C.7 Capacitance and Current DLTS setup schematic . . . . .	75
C.8 Capacitance and current DLTS setup in laboratory . . . . .	76
D.1 LabVIEW sweep interface. . . . .	77

# List of Tables

4.1	Sample cleaning procedure.	15
4.2	Spin coating parameters.	16
4.3	Evaporation process parameters	17
4.4	ModuLab parameters used for IV and CV measurements.	20
4.5	Solar simulator parameters for IV measurements with AM1.5G conditions.	21
4.6	Extracted device parameters of four different solar cells	21
5.1	Single transient settings for LabVIEW program.	33
5.2	Voltage sweep parameters in the LabVIEW framework.	34
5.3	Single transient settings for LabVIEW program.	35
5.4	Sweep temperature parameters in the LabVIEW framework	36
5.5	PID controller parameter.	40
6.1	Time scales used for the first experiment.	41
6.2	Measurement Parameters for Second Experiment.	43
A.1	Database for colloidal solar cells (1)	66
A.2	Database for colloidal solar cells (2)	67
A.3	Database for colloidal solar cells (3)	68
C.1	Specifications of Agilent 33522 arbitrary waveform generator (AWG).	71
C.2	Specifications of Janis ST-500 cryostat.	72
C.3	Specifications of LakeShore 335 temperature controller.	72
C.4	Specifications of Boonton 72 capacitance meter.	73
C.5	Specifications of Femto DHPCA transimpedance current amplifier.	74
C.6	Specifications of Rohde and Schwartz RTM1054 oscilloscope.	74
D.1	Additional LabVIEW settings	78



# Chapter 1

## Introduction to Colloidal Quantum Dot Solar Cells

### 1.1 Third Generation Solar Cells

Climate change, scarcity of resources, and dependency on fossil fuels are important challenges to the society of today. A trend towards renewable energies is apparent, not only to save the environment, but also to guarantee the needs of future generations [36]. Besides hydroelectricity, wind energy, wave power, and geothermal energy, solar energy represents one of the most promising energy sources, which can be directly converted into electricity. Photovoltaics (PV) are the driving technology behind this conversion and solar cells (SC) contain a photovoltaic material.

The first generation SCs were made of poly- or monocrystalline silicon wafer. Despite efficiencies around 25% [25], which is close to their theoretical limit (Shockley-Queisser-limit [52]) of 33.7%, they require high purity materials and therefore suffer from high manufacturing costs. Second generation SCs exhibit the potential for low-cost manufacturing by depositing thin film absorbers (amorphous silicon, CdTe, or CIGS) onto large area, flexible substrates. However, efficiencies are typically at least 4% lower [25].

Third generation solar cells attempt to unify both, low manufacturing cost and high efficiencies. Nanomaterials play an important role due to the recent advance in colloidal syntheses. A nanocrystalline (NC) thin film of colloidal quantum dots (cQD) is obtained by solution-processing (spin coating or dip coating) allowing low-cost manufacturing in a roll-to-roll fashion. In this thesis we use *cQD* to refer to the active particles and *NC film* to refer to the cQD solid thin film. The thin film consists of several layers of QDs. Their band gap is tunable across a wide range by varying the diameter of the QDs, which can be easily controlled during synthesis. This allows the solar cell to be sensitive in the near infra-red wavelengths, where approximately half of the solar spectrum is concentrated [49].

A drawback with colloidal synthesized QDs is the existence of long organic ligands, which build an insulating shell around the QDs and thereby decrease the inter-QD coupling [26]. The long ligands are typically replaced with shorter ones, by soaking the NC film in a chemical reagent [2,57].

## 1.2 PbS Schottky Solar Cells

Most of today's mass produced solar cells consist of a silicon pn-junction (i.e. a p-doped and a n-doped silicon layer on top of each other). Photons are absorbed near the pn-junction, or space charge region (SCR), where they generate electron-hole pairs. Opposite carriers are pushed away due to the electric field in the SCR, thereby contribute to the photocurrent [55].

Instead of using two doped semiconductors, solar cells can also be made of metal-semiconductor junctions, or Schottky-junctions. At the interface a so called Schottky-barrier is formed, responsible for the typical rectification characteristic [53].

In recent years, Schottky solar cells based on QDs have been investigated by sandwiching QD layers between two electrodes with different work functions. Such devices were successful fabricated for PbS [2,3,10,58], and PbSe [8,22], with power conversion efficiencies measured up to 3.6% [10]. In this thesis, we use PbS QDs since it show better stability in air than PbSe QDs.

## 1.3 Motivation for Trap Investigation

cQD-based solar cells represent a relatively new technology compared to their silicon counterparts. NC semiconductors are not well characterized yet but due to their great features, the urge to understand material properties and device mechanism has increased during the last couple years.

A phenomenon that influences the electrical properties of a device are deep-level traps. They are states within the band gap, which are able to capture both electrons and holes from conduction and valence band, respectively [55]. Deep traps thereby modify various device parameters considerably. During the time a carrier is trapped, it cannot flow through the material and contribute to a current. Therefore the mobility and also the conductivity are decreased [40]. Another major effect of trapping are longer carrier lifetimes, so that the photocurrent persist after an excitation has ceased [19].

When traps affect electronic properties in an uncontrolled manner, they are extremely undesirable. They have been thoroughly investigated in silicon and germanium, but not in NCs. By finding appropriate methods to detect and characterize traps in NCs, it would be possible to understand how to systematically tune the device parameters. In this thesis, a commonly used method, deep-level transient spectroscopy (DLTS), is investigated with the goal to observe and analyse deep-level traps in solar cells based on cQDs.

## 1.4 Thesis Outline

This thesis is organized as follows: Chapter 2 summarizes a selection of approaches that were developed to detect traps during the last 60 years. An overview of the theoretical background used for this thesis is given in Chapter 3. Chapter 4 explains fabrication steps together with the characterisation of PbS solar cells. In Chapter 5, the set up developed for DLTS measurements is explained in detail. The subsequent measurements and results are discussed in Chapter 6. Chapter 7 summarizes the results of this work.

## Chapter 2

# Review of Techniques for Electronic Trap State Investigation

In the following section, several approaches developed to investigate electronic traps during the past 60 years are discussed.

Historically, the earliest experiments to investigate electronic traps were studies on phosphors with *glow curves* reported in Ref. [44] from 1945. The sample under test is cooled down to typically 77 K, illuminated with ultraviolet light to fill traps with electrons, and then heated at a constant, slow temperature rate. With increasing temperature, electrons can gain enough energy to be thermally stimulated into the conduction band, when emitted from the trap. The thermally ejected electrons stimulate the phosphor and the phosphorescence is recorded as a function of temperature. For different heating range, characteristic temperatures where the (glow) intensity reached a maximum were observed enabling to determine the depth and density of traps.

Thermally stimulated capacitance (TSCAP) and current (TSC) measurements are two modifications of glow curve measurements. The sample is again cooled, and traps are filled either optically or electronically. Then a reverse bias is applied, the temperature is ramped up, and the steady-state capacitance or current is measured. The carriers emitted from traps are observed either as capacitance steps [47] or current peaks [19, 48].

In the period between 1966 and 1974, trapped charge species were detected mainly in the form of capacitance and currents. In early steady-state measurements, the initial capacitance and the steady-state capacitance were compared to obtain the deep-level trap density [14, 47, 62]. Afterwards, transient behaviour of capacitances and currents after an applied filling pulse were investigated [42, 46]. While the characteristic energy (temperature) of the system is changed, signal peaks were observed belonging to trap specific time constants. These single-shot measurement techniques were tedious, time-consuming and do not allow different traps to be resolved.

In 1974 Lang proposed a new method, deep-level transient spectroscopy (DLTS) [34], that uses automated data acquisition techniques to overcome the problems emerged in former approaches. For this method, Lang introduced the *rate window* concept, where the acquired transient signals are correlated by an integrator filter after weighted with a corresponding weighting function. As in the former approaches, a change in transient behaviour with temperature is observed. The output of the filter, also known as a DLTS

spectrum, reaches a peak when the decay rate of the measured transient signal passes the rate window (or characteristic time constant) of the filter. By changing the rate window, time constants belonging to different transient signals can be measured. Together with the temperature of the corresponding DLTS spectrum peak, the extracted time constants can be directly used to obtain characteristic parameters of traps (i.e. their activation energy and capture cross-section).

Due to its great success in the field of trap detection, several refinements of the original DLTS approach have been developed. In double-correlation DLTS (DDLTS) [37], two different fill-pulse amplitudes are used, allowing the traps within a spatial window to be detected. This enables the investigation of density profiles. In constant capacitance DLTS (CCDLTS) [30], the capacitance is held constant during the measurement by varying the applied voltage with the help of a feedback loop. Lock-in Amplifier DLTS [31] and correlation DLTS [39] differ from the original approach only in other weighting functions, but feature better signal to noise ratios. Laplace DLTS [23] and Fourier DLTS [60] originate due to the possibility of storing measured data electronically for further processing. Together with other signal processing approaches, they are summarized in the term of computer DLTS [27], which is equivalent to many historic DLTS variants.

The original DLTS method measured capacitance transients. Since carriers emitted from traps can also be detected as currents or charges, current DLTS and charge DLTS methods were developed [16, 24].

All the methods presented above are mainly designed to extract the trap activation energy, the capture cross section, and the density of traps. To determine other important parameters, the following methods have been developed. With admittance spectroscopy [51], positron annihilation spectroscopy (PAS) [56], and open-circuit voltage decay [50] the carrier lifetime can be determined. The latter approach also enables the investigation of series resistance. Optical DLTS can be used to determine optical trap parameters such as optical cross-section [33] or to create electron-hole pairs for minority-carrier investigations, for example with photo-induced current transient spectroscopy (PITS) [28].

# Chapter 3

## Theory of Deep-Level States in Semiconductor Materials

This section provides a theoretical background of deep-level states. After an introduction in Section 3.1 and Section 3.2 a mathematical treatment is given by considering the carrier dynamics in a semiconductor material in Section 3.3. How carriers are detected within the space charge region is described in Section 3.4. The specific case of deep-level transient spectroscopy (DLTS) and its variations are then discussed in Section 3.5.

### 3.1 Defects

A simplified band diagram of a semiconductor with perfect single-crystal material and therefore perfect geometric lattice periodicity is shown in Figure 3.1(a). It consists of the valence and the conduction band separated by a band gap, where no electronic states exists. Transitions of electrons from one band to the other can therefore only take place by direct band to band transitions.

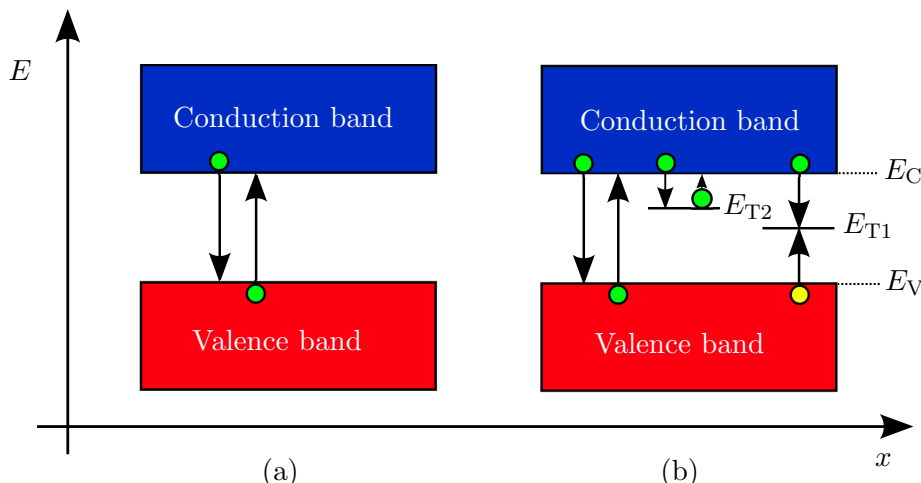


Figure 3.1: Band diagram of an ideal semiconductor material (a) and a real semiconductor material (b). Electrons are indicated in green, whereas holes are yellow. The two traps states have energies  $E_{T1}$  and  $E_{T2}$ , respectively.

However, in reality this perfect periodicity is disrupted by either foreign atoms (impurities) or crystalline defects, such as vacancies, interstitials, edge dislocations or stacking faults [40]. These imperfections create discrete energy states within the band gap, as shown in Fig. 3.1(b), which are known as *trap states* or simply *traps*.

## 3.2 Deep-Level Traps

A distinction is made between two type of traps: states near the band gap (shallow-level traps) and states deep in the band gap (deep-level traps). Energy states are called *deep* when their distance from either the band edge is more than 0.1 eV at room temperature. In this thesis, only the latter are discussed.

Since energy states can be occupied by charge carriers, transitions are possible from the band edges to the states and vice versa. The interaction of carriers with traps change the electrical properties of the material. In turn electrical measurements can be used to extract important physical parameters. The most important expressions hereof are presented in the following, whereas their derivation are given by Sah et al. in Ref. [48].

## 3.3 Shockley-Reed-Hall Theory

One way to describe the properties of deep-level traps is to consider only one impurity at a distinct energy level  $E_T$  as shown in Figure 3.2. The semiconductor exhibits a free electron density  $n$  in the conduction band and a hole density  $p$  in the valence band, introduced by shallow-level dopants.  $n_T$  and  $p_T$  are the density of traps occupied by electrons and holes, respectively. The total density of traps,  $N_T$ , is therefore  $N_T = n_T + p_T$ . All densities are given in [ $\text{cm}^{-3}$ ].

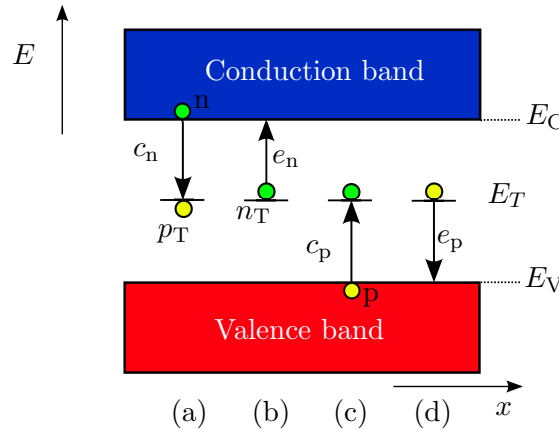


Figure 3.2: Four fundamental processes for a distinct trap energy level with energy  $E_T$ : Electron capturing (a), electron emission (b), hole capturing (c) and hole emission (d)

After the Shockley-Read-Hall theory, there are four basic processes that may occur at this single trap [15]:

- The capture of an electron from the conduction band by an empty trap
- The emission of an electron occupying a trap back to the conduction band
- The capture of a hole from the valence band by a trap containing an electron
- The emission of a hole from a neutral trap back to the valence band

Each of the above processes is characterized by a rate quantity. As indicated in Figure 3.2,  $e_n$  and  $e_p$  represent the emission rates, whereas  $c_n$  and  $c_p$  the capture rates for electrons or holes, respectively. In the following, only equations for electrons are treated, because many relations are analogous for electrons and holes.

The capture coefficient  $c_n$  is given in a semi-classical model by

$$c_n = \sigma_n v_{th}, \quad (3.1)$$

where  $\sigma_n$  is the electron capture cross-section and  $v_{th}$  is the electron thermal velocity. An expression for the emission coefficient as a function of temperature is given by

$$e_n = c_n n \exp((E_T - E_F)/kT) \quad (3.2)$$

For a non-degenerated semiconductor, the free electron concentration  $n$  can be expressed as

$$n = N_c \exp(-(E_c - E_F)/kT), \quad (3.3)$$

with  $N_c = 2(\frac{2\pi m_n k T}{h^2})^{3/2}$  the effective density of states in the conduction band.

Based on Equation 3.1, 3.2 and 3.3 we can calculate the *emission time constant* as:

$$\tau_e = 1/e_n = \frac{\exp((E_c - E_T)/kT)}{T^2 \gamma_n \sigma_n}, \quad (3.4)$$

where  $\gamma_n = (v_{th}/T^{1/2})(N_c/T^{3/2})$  is a material specific constant.

Equation 3.4 is a so called modified Arrhenius law<sup>1</sup>. It shows the dependence of the emission time constant on the temperature  $T$ , which can be exploited to study deep-level traps. For high temperatures, the time constant is small and for low temperatures the time constant increases.

A more convenient way to write the equation is

$$\ln(\tau_e T^2) = \frac{E_c - E_T}{kT} - \ln(\gamma_n \sigma_n) \quad (3.5)$$

Equation 3.5 has the form of a straight line. A plot of  $\ln(\tau_e T^2)$  versus  $1/T$  has a slope of  $(E_c - E_T)/k$  and intercept on the  $\ln(\tau_e T)$  axis of  $\ln(1/(\gamma_n \sigma_n))$ . Knowing the emission time constant at different temperatures can be used to determine the activation energy and capture cross-section of a trap.

As mentioned in Section 3.2, traps emitting or capturing charge carriers are charged or neutral. Any technique that detect charged species can be used to analyse their dynamic behaviour and therefore to extract their time constants.

<sup>1</sup>[http://en.wikipedia.org/wiki/Arrhenius\\_equation](http://en.wikipedia.org/wiki/Arrhenius_equation)

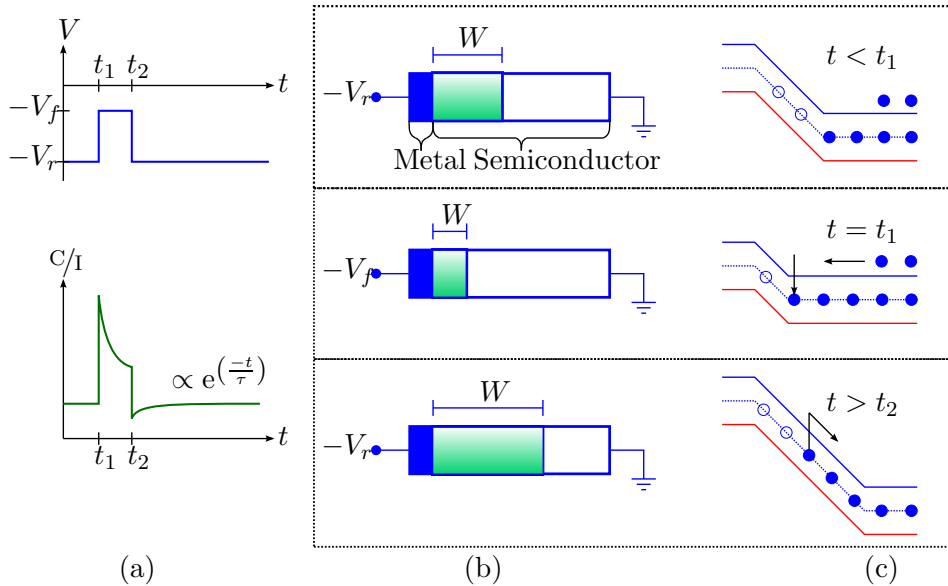


Figure 3.3: Transient measuring procedure. Applied pulse and resultant transient are shown in (a), a schottky diode at steady-state, forward and reversed bias in (b) and the band diagram thereof in (c)

### 3.4 Space Charge Spectroscopy

In this thesis we use the technique of space charge spectroscopy to characterize deep levels, where trapped charges are detected by measuring the capacitance or the current of the space charge region (SCR) of a Schottky diode. Both methods are explained in the next two sections. A third possible method, or charge measurement [24], is not discussed here, since only the other two methods are used.

#### 3.4.1 Capacitance Measurement

Figure 3.3 shows the procedure of a capacitance measurement of a Schottky diode on a n-type substrate. At the beginning, it is assumed that a steady state condition has been reached for  $t < t_1$ , by applying a reverse voltage for long enough at the metal contact of the diode. All traps in the SCR are empty as indicated right on top of Figure 3.3(c). When the diode is pulsed from reverse to zero bias, carriers will flow into the SCR, thereby reducing its width  $W$ . The capacitance is increased, when considered as a parallel plate capacitance given by

$$C = \frac{\epsilon A}{W}, \quad (3.6)$$

where  $A$  is the diode area and  $\epsilon$  the effective permittivity.

As the empty traps begin to capture the carriers, the width widens and capacitance decreases, until emission and capture processes balances each other. At  $t = t_2$ , the bias voltage is switched back to reverse bias increasing the potential energy on the left bands. Carriers, that are not trapped within the SCR, are swept away immediately by the electric field leading to a rapid increase of  $W$  and to a fall of  $C$  (Figure 3.3(a)). Carriers that are still trapped, however, will continuously empty the traps by thermal emission processes with the emission rate  $\frac{1}{\tau_e}$ .

The time dependence of the trap occupation density is given as

$$n_T(t) = N_T \exp\left(-\frac{t}{\tau_e}\right). \quad (3.7)$$

Here we assume  $e_n \gg e_p$  as in Ref. [50], so that only traps in the upper half of the band gap are considered.

During this emission process, the change of the SCR width leads to a time-varying capacitance according to Equation 3.6. In the steady state, a capacitance  $C_\infty$  is reached. These time-varying capacitances are also referred as capacitance transients and are related to the trap density as

$$C(t) = C_0 \sqrt{1 - \frac{n_T(t)}{N_D}}, \quad (3.8)$$

where  $N_D$  is the donor doping density. Using a first order approximation of the last equation and substituting  $n_T(t)$  by Equation 3.7 results in an exponential time dependence expression as

$$C(t) = C_0 \left[ 1 - \frac{n_T(0)}{N_D} \exp\left(-\frac{t}{\tau_e}\right) \right] \quad (3.9)$$

### 3.4.2 Current Measurement

Instead of capacitance measurements carriers emitted from deep traps can also be detected as current flowing through the space charge region. The measurement protocol is the same as described in Section 3.4.1. Current measurements are more complicated, because the measured current actually consists of three subcurrents: the emission current  $I_e$ , the junction leakage current  $I_l$ , and the displacement current  $I_d$ . For  $n_T \ll N_D$  and  $n_T(0) \ll N_D$  a similar relation as for the capacitance can be found:

$$I(t) = \frac{qAW_0}{2\tau_e} n_T(0) \exp\left(-\frac{t}{\tau_e}\right) + I_l \quad (3.10)$$

where  $W_0$  is the steady state SCR width and  $A$  the device area.

### 3.4.3 Temperature Effect on Capacitance and Current Measurements

For capacitance transients given in in Equation 3.9, the only quantity that is temperature dependent is the time constant. Therefore, the initial capacitance step remains the same for all temperatures. For current transients, however, the effective amplitude is inversely proportional to the time constant (see Equation 3.10). For high temperatures, the time constant is small, and therefore the initial current is high. For low temperatures, time constants are big and the initial current is small. This makes current measurements difficult at low temperatures.

In principle, necessary time constants can be obtained directly from measured capacitance or current transient, e.g. by an exponential fit of each curve or by an Arrhenius plot from each transient. When the number of time constants contributing to a single transient are not known *a priori* or the the steady state value cannot be reached within a measurement period [51], the first approach is not useful.

A different approach was performed by Sah et al. in early studies of impurities [46] and is tedious and time-consuming, since for each transient the time constant has to be extracted from an individual Arrhenius plot (single-shot measurements). Additional to speed considerations, early techniques had a lack of sensitivity and spectroscopic nature, in the sense that no distinction between different traps could be made.

### 3.5 Deep-Level Transient Spectroscopy (DLTS)

In 1974, David Lang invented a new method to characterize deep-level impurities to overcome these problems. It was the first method to use automated data acquisition techniques and is called deep-level transient spectroscopy (DLTS) [34].

This method was also used in this thesis to investigate deep traps in solar cells based on nanocrystals. Its main properties are explained in Section 3.5.1 by considering first Lang's original double Boxcar approach or Conventional DLTS. Several variations that have been developed up to now are briefly discussed in Section 3.5.2.

#### 3.5.1 Conventional Boxcar DLTS

The original DLTS method is based on the space charge spectroscopy technique discussed in Section 3.4. A pulse signal is applied to a diode at various temperatures obtaining emission transients with different time constants as indicated in Figure 3.4.

The concept that Lang introduced is a signal-processing technique, where the measured signals  $f(t)$  (i.e. transients) are correlated by a weighting function  $w(t)$ . The output of such a correlation filter with integration period  $P$  is given by

$$S = \frac{1}{P} \int_0^P f(t)w(t)dt \quad (3.11)$$

and is called a DLTS spectrum.

A boxcar filter measures the amplitude difference from two distinct times,  $t_1$  and  $t_2$ , of a signal. The weighting function can therefore be written as

$$w(t) = \delta(t - t_1) - \delta(t - t_2), \quad (3.12)$$

where  $\delta$  is the Dirac delta function. For a monoexponential decaying capacitance signal  $C(t)$  with a emission time constant  $\tau_e$ , the DLTS spectrum has the following form

$$S = C(t_1) - C(t_2) = \exp\left(-\frac{t_1}{\tau_e}\right) - \exp\left(-\frac{t_2}{\tau_e}\right). \quad (3.13)$$

$S$  is depicted in Figure 3.4 and has a maximum when the time constant of the transient  $\tau_e$  is equal to the so called time window or reference time constant [34]

$$\tau_{e,\max} = \frac{t_2 - t_1}{\ln(t_2/t_1)} =: \tau_{\text{ref}}. \quad (3.14)$$

This expression is valid for capacitance transients, for current transients the time window it is given as

$$\frac{t_2 - t_1}{\tau_{\text{ref}}} = \ln\left(\frac{1 - t_2/\tau_{\text{ref}}}{1 - t_1/\tau_{\text{ref}}}\right) \quad (3.15)$$

By varying the time window, different DLTS spectra yield a maximum with a corresponding time constant and temperature, giving one point pair for the Arrhenius plot (see Section 3.4). This is commonly done for a fixed ratio  $\frac{t_2}{t_1}$ .

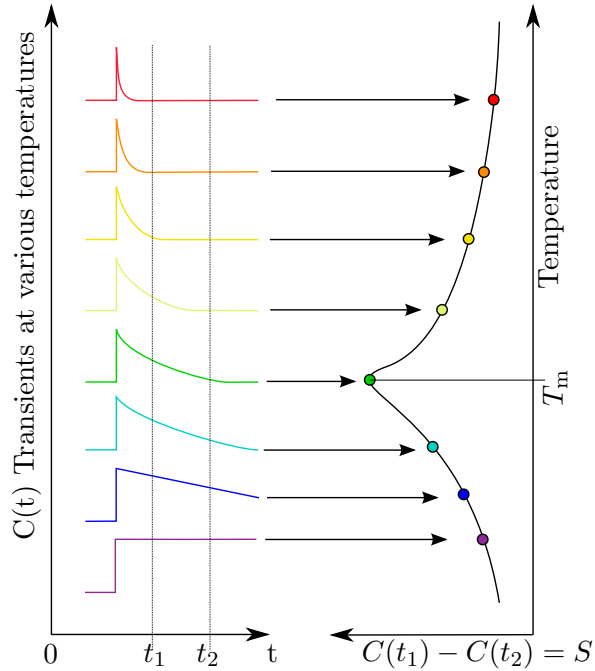


Figure 3.4: Scheme of the Boxcar method. Transients at various temperatures with different time constants are depicted on the left. On the right is the corresponding DLTS spectrum given as the difference of the two sampling point on the left. The maximum point is at temperature  $T_m$

### 3.5.2 Other DLTS Methods

Several variations of the Boxcar DLTS technique have been developed in the past. Schroder gives a good overview in Ref. [50], whereas Milnes treats them in more detail [40]. In the following, only a selection of variations are discussed.

#### Gaussian Boxcar approach

The Gaussian Boxcar approach is a Boxcar approach coupled with a Gaussian filter. Schulz reported a similar method, where the a square filter averages the transient at the two sample times of the Boxcar filter over a distinct time interval [51].

The filter here consists of two Gaussian pulses with their mean at the two sample times,  $t_1$  and  $t_2$ . The weighting function is defined as:

$$w(t) = \exp(-(t - t_1)^2/2\sigma^2) - \exp(-(t - t_2)^2/2\sigma^2) \quad (3.16)$$

**Exponential approach**

It has been shown, that for single decaying exponential functions the optimum weighting function has the form of a decaying exponential as well [39]. In this thesis the current DLTS version of this approach was implemented. Its DLTS spectrum is calculated by

$$S = \int_{\tau_h}^{\tau_m} I(t) \exp(-t/\tau_r) dt, \quad (3.17)$$

where  $\tau_h$  is the holding time after the pulse,  $\tau_r$  is the restoration time constant, and  $\tau_m$  is the restoration time constant ( $\tau_m = 2.06\tau_r$  for optimum output) [13]. At each filter process, the transient signal is base-line restored at  $\tau_m$  and then integrated from the holding time time to this restoration time.

In conventional approach described above, only two sampling points per transient are evaluated for a distinct weighting function. Due to the weighting function explained here, more points per transient flow into the correlation and enhances there for the accuracy and signal to noise ratio.

**Fourier DLTS**

Fourier analysis was also applied to DLTS as proposed in Ref. [29]. In this so called Fourier DLTS method, the measured transients are correlated in the same way as explained above, with the difference that the weighting functions are sinusoidal leading to the following correlations

$$a_n = \frac{2}{P} \int_0^P I(t) \cos\left(\frac{2\pi n t}{P}\right) dt \quad (3.18)$$

$$b_n = \frac{2}{P} \int_0^P I(t) \sin\left(\frac{2\pi n t}{P}\right) dt \quad (3.19)$$

$a_n$  and  $b_n$  correspond to the n-th order Fourier Series coefficient of the measured transient and  $T$  is the integration period. Weiss showed in his work that the time constant of a exponential decaying transient can directly be calculated by the ratio of two Fourier coefficients [60]. Four methods are possible, whereas in this thesis the following formula is used

$$\tau_e(a_n, b_n) = \frac{P}{2\pi n} \frac{b_n}{a_n} \quad (3.20)$$

and only the lowest order is considered, i.e.  $n = 1$ , according to the observations made in Ref. [29].

# Chapter 4

## Device Fabrication and Characterization

This chapter describes the sample preparation of colloidal solar cells and their characterization. The preparation is explained in Section 4.1, and the characterization is discussed in Section 4.2.

### 4.1 Sample Preparation

#### 4.1.1 Materials

All materials used for the sample preparation as well as for the substrate cleaning are listed and described here:

- Acetone: Acetone is used here to clean the substrates.
- Acetonitrile: Acetonitrile is used reduce aggregates after the ligand exchange by flushing residuals away.
- Aluminium (Al): Aluminium is used as a component for the cathode of the sample. It has a low workfunction.
- Ammonium Thiocyanate ( $\text{NH}_4\text{SCN}$ ):  $\text{NH}_4\text{SCN}$  is an inorganic compound and is used to replace long insulating ligands around quantum dots (QD) [1]. This enhances inter-particle coupling in QD solids preferable for device applications.
- 1,4-Benzenedithiol (BDT): BDT is, like ammonium thiocyanate, used to replace ligands. In contrast to  $\text{NH}_4\text{SCN}$ , it is an organic compound and establishes a cross link between QDs [2].
- Detergent: During cleaning a universal detergent (Mucasol) is used.
- DI-water: DI-water is used to clean and rinse the substrates from isopropanol residuals (see below).
- Ethanedithiol (EDT): EDT is the third alternative for the ligand exchange used in this thesis. As BDT it is a an organic compound, but is a lighter, and therefore vaporized faster than BDT.

- Indium Tin Oxide (ITO): ITO is a solid solution of indium oxide and tin oxide and is used here as the transparent anode of the solar cell.
- Isopropanol: Isopropanol is used for the cleaning of the substrates.
- Lead sulfide (PbS): Lead sulfide is a semiconductor and is used as the nanocrystal material or the active layer in the schottky solar cell produced in this thesis. For the same purpose it was used in Refs. [2–4].
- Lithiumflouride - (LiF): Lithium fluoride is the lithium salt of hydrofluoric acid and is used in this thesis as a protection layer between the Al and PbS layer to enhance stability and performance. Various explanations therefor are discussed in Refs. [5–7].
- Silver (Ag): Silver is the third cathode material beside Al and LiF. It has a better air stability with respect to Al. Using Ag as uppermost layer increases the life time of a cell twelvefold [3].

#### 4.1.2 Preparation Procedure

For the purpose of investigating defects, thin film solar cells based on Schottky barriers are fabricated. The device structure and the band diagram are depicted in Figure 4.1. In this thesis, PbS QD layers were sandwiched between two electrodes to get a Schottky-junction as reported in Refs. [2, 3].

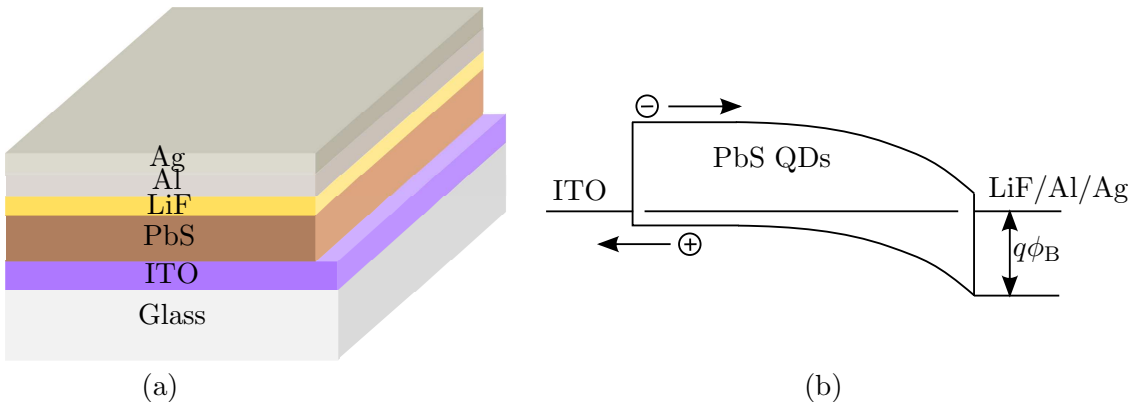


Figure 4.1: Structure of the produced samples (a) with the equilibrium band diagram (b).  $q\phi_B$  is the Schottky barrier height.

Each sample is fabricated on an ITO coated glass substrate (12mm by 12mm from thin-film devices, Annaheim, CA). The ITO anode was patterned onto the glass by lithography.

#### Sample cleaning

To remove dust and particles on the surface, each ITO-glass substrate was cleaned according to the procedure given in Table 4.1.

Step	Solvent / Method	Time	Sonicate	Remark
1	Detergent (1%)	5 min	yes	2 iterations
2	DI water	5 min	yes	2 iterations
3	Acetone	5 min	yes	2 iterations
4	Isopropanol	5 min	no	boiling
5	N <sub>2</sub> blow drying	-	no	-

Table 4.1: Sample cleaning procedure.

### Plasma treatment

After the cleaning steps with solvents, organic residuals left on the substrates are removed by an O<sub>2</sub> plasma treatment in a plasma generator. After putting the samples inside the chamber, the pressure is turned down while oxygen is pumped in. When the pressure stabilizes at around 0.3 mbar, the plasma is ignited. For the used ITO-glass substrates, the power was set at 30 W and the timer to 300 seconds.

### Active layer deposition

In a next step, the active layer is deposited onto the ITO coated glass. In this thesis, we used two layer-by-layer methods to fabricate homogeneous and crack-free films: dip-coating [8] and spin-coating [9, 10]. All the concentrations and solutions used for each produced solar cell can be found in Appendix A.

- Dip coating: The first three samples were produced with the dip coating method. A layer of NC is deposited on the ITO surface by consecutively dipping the substrate into different solutions. Figure 4.2 summarizes three processes performed during the beginning of thesis and are described hereafter:

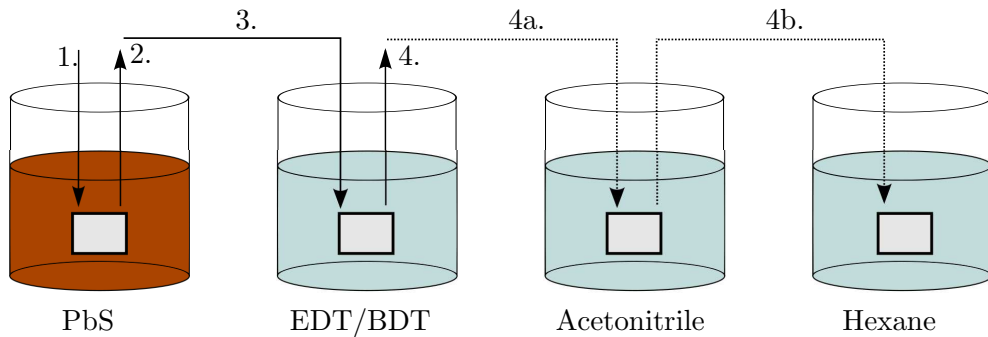


Figure 4.2: Dip coating procedure with the different solutions, where the sample is immersed in. The process is explained in the text.

1. Immersion: The substrate is immersed in the PbS-Hexane mixture at a constant speed. It remains there for 1 second.
2. Deposition: The substrate is pulled up and a film is deposited by itself.
3. Ligand exchange: The substrate is immersed into EDT for 5 seconds to exchange the ligands.

4. Drying: The substrate is dried in air for about 5 seconds.
- 4a. Rinsing step 1: The substrate is rinsed in acetonitrile for 1 second.
- 4b. Rinsing step 2: The substrate is rinsed in hexane for 1 second.
5. Repeat all previous steps.

Step 4a and 4b are additional rinsing steps tried to reduce the building of aggregates.

- Spin coating: In contrast to dip coating, a small amount of the NC solution is dropped on the substrate, which is immediately rotated at a high speed. The parameters used in this thesis are:

Spin time [s]	velocity [rpm]	acceleration [rpm/s]
60	4000	2000

Table 4.2: Spin coating parameters.

A scheme of the procedure is given in Figure 4.4, whereas the spin-coating set up is depicted in Figure 4.3. The procedure is described as follows:

1. Fixing: The substrate is fixed on the sample holder of the spin-coater. Then the vacuum is turned on to hold the sample while it rotates.
2. Deposition: Several drops of PbS-Hexane solution is dropped onto the substrate to cover the whole ITO layer.
3. Spinning: The substrate is rotated for 30 seconds. This movement flushes the solution away and leads to a homogeneous film thickness depending on the entered parameters.
4. Ligand exchange: The substrate is immersed into EDT, BDT or NH4SCN solutions for about 30 seconds to exchange the ligands. The substrate is orientated upside down.
5. Rinsing step: The substrate is rinsed in acetonitrile for 1 second.
6. Repeat all previous steps.

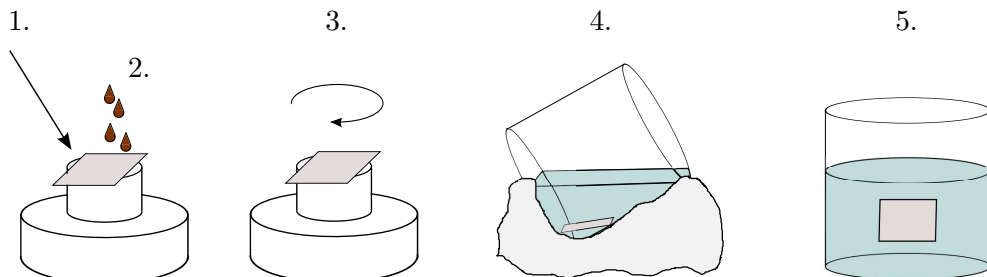


Figure 4.3: Spin coating procedure steps: Fixing onto holder (1), deposition of solution (2), spinning (3), ligand exchange (4) and rinsing step(5).

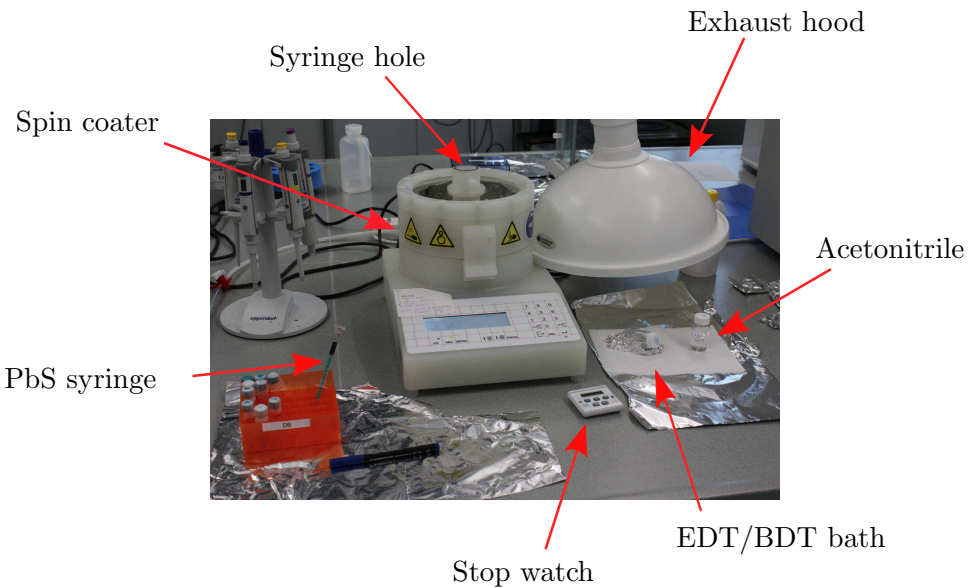


Figure 4.4: Spin coating set up with spin coater and solutions.

### Post processing

After the film deposition, a small strip (ca. 2 mm) of the active layer was removed around the entire sample area to uncover the connections to the ITO anode.

### Cathode evaporation

The final step is the evaporation of the remaining three layers building the cathodes, i.e. LiF, Al, Ag. The process parameters are summarized in Table 4.3.

Evaporation parameters			
Material	Parameter	Value	Remark
LiF	Rate	0.03 Å/s	-
LiF	Thickness	1 nm	-
Al	Power for ramp 1	48%	Time: 4:00 + 4:00, Warmup
Al	Power for ramp 2	45%	Time: 2:00 + 0:15, Warmup
Al	Max power	55%	Burnout
Al	Thickness	100 nm	-
Al	Deposition rate	0.2 Å/s (first 10 nm)	1.5 Å/s (rest)
Al	Cooldown idle ramp	2:00	-
Ag	Rate	2 Å/s	-
Ag	Thickness	300 nm	-

Table 4.3: Evaporation process parameters

Figure 4.5 shows three homogeneous and crack free PbS solar cell films after a spin coating procedure and a final solar cell with evaporated cathodes. The design used in this thesis has ten devices and two ground connections.

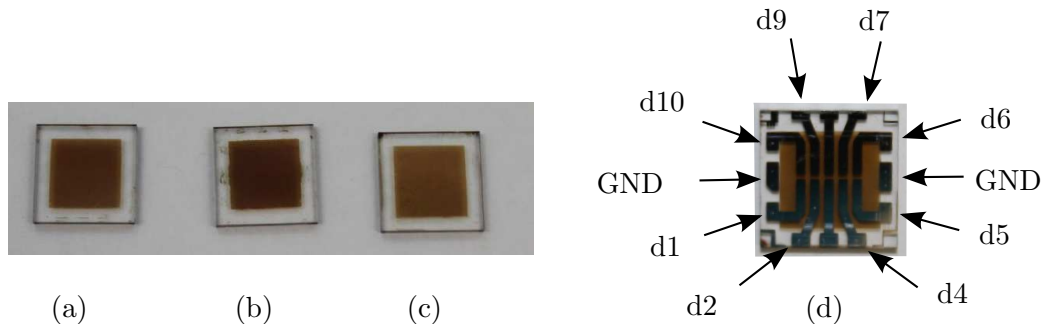


Figure 4.5: Finished colloidal PbS films. Film (a) is a 10 layer BDT solar cell, (b) a 15 layer BDT cell and (c) a 10 layer EDT cell. A final solar cell is shown in (d).

#### 4.1.3 Remarks and Conclusions

As mentioned in the last chapter, first three samples were produced by a dip coating process, where the dip coater has to be operated manually. It took 4-5 minutes per cycle and therefore almost 2.5 hours per sample. In contrast to that, manual spin coating is three times faster. An automatic dip coater was designed to reduce time in the laboratory (see Appendix B).

Several observations were made during sample preparation with spin coating:

- The spinning has to start immediately after PbS-Hexane drops fell onto the substrates. Otherwise, rings and spots will be formed on the surface yielding a non-uniform film.
- The transition from the ligand solution to anhydrous acetonitrile has to be as fast as possible. If too much time elapses, the film will dry out and the layer is prone to cracks. Putting then the sample into acetonitrile will destroy the film as depicted in Figure 4.6. A partial delamination could be observed, especially on regions where no ITO was deposited.

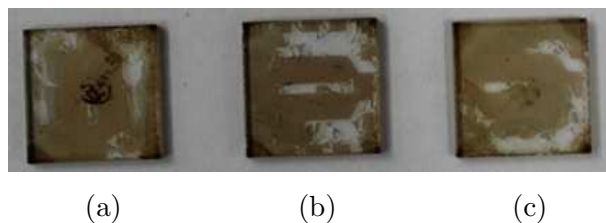


Figure 4.6: Three samples with partially detached films. An EDT sample after two layers (a), a BDT sample after 3 layers (b) and another BDT sample after 3 layers (c).

- During this thesis different combinations with the involved solutions were tried. Finally, the following solutions and concentrations were adopted:
  - PbS: PbS is mixed with hexane to obtain a 2 ml-mixture with a concentration of 5 mg/ml.
  - EDT: 8.39  $\mu$ l of pure EDT is mixed with 1 ml acetonitrile leading to a 0.1 M solution. With 80  $\mu$ l of the 0.1 M solution and 3.92 ml acetonitrile, an EDT solution with final concentration of 0.2 mM is obtained.
  - BDT: 14.2 mg/ml of pure BDT is diluted in 1ml acetonitile leading to a 0.1 M solution. With 80  $\mu$ l of the 0.1 M solution and 3.92 ml acetonitrile, a BDT solution with final concentration of 0.2 mM is obtained.
  - Acetonitrile: 10 ml of anhydrous acetonitrile is used and exchanged after 10 layers.

## 4.2 Characterization of PbS Solar Cells

### 4.2.1 Measurement Setup

To characterize the samples, current-voltage (IV) and capacitance-voltage (CV) measurements were performed concurrently at room temperature in ambient air, using a ModuLab MTS Source Measure Unit (SMU). Together with dark measurements, illuminated IV-curves were also acquired to investigate the solar cell parameters. The samples were illuminated using an Oriel AM1.5G solar simulator, where the incident light had an intensity of  $100 \text{ mW/cm}^2$ . The setup is given as a schematic in Figure 4.7 and the measurement parameters in Table 4.4 and Table 4.5. The parameters for the monochromator are set in a LabView program.

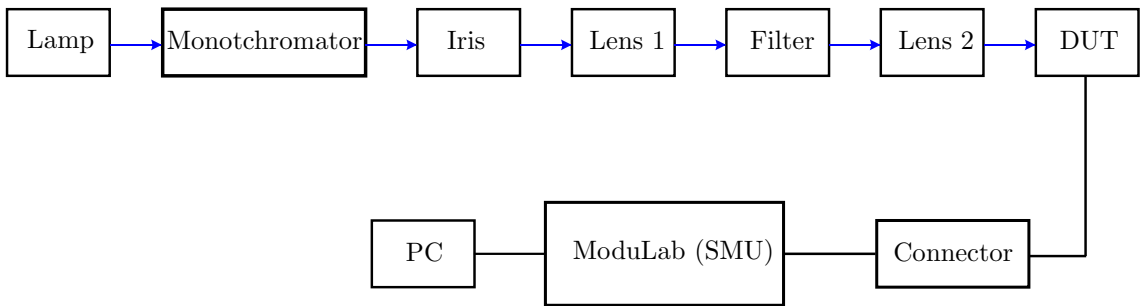


Figure 4.7: IV measurement setup scheme. The illumination of the sample is shown in blue, and the electrical signal flows from the device under test (DUT) towards the computer.

ModuLab Parameters		
Group	Parameter	Value/Setting
Hardware Requirements	Experiment type	Normal
Hardware Requirements	Instrument config	Mat only
Sample Setup	Electrode Area	$0.0172 \text{ cm}^2$
Sample Setup	Thickness	1 mm
Instrument Exp. Setup	Connections	4 Terminal
Experiment step	Linear sweep impedance	-
Scan setup	Start level	-0.7 V
Scan setup	End Level	0.7 V
Scan setup	Scan rate	10 mV/s
Impedance Setup	Measurement mode	Sample only
Impedance Setup	Technique	Single frequency
Impedance Setup	Amplitude (rms)	10 mV Absolute
Impedance Setup	Frequency	100 kHz
Impedance Setup	Repeat every	5 mV

Table 4.4: ModuLab parameters used for IV and CV measurements.

Solar simulator parameters		
Device	Parameter	Value/Setting
Monochromator	Serial	0
Monochromator	Wavelength	0
Monochromator	Filter	No filter
Monochromator	Grating	Mirror
Iris	Opening	8mm at sample plane
Lens 1	Focus	50mm
Lens 2	Focus	75mm
Lens 1 and 2	Distance	125mm

Table 4.5: Solar simulator parameters for IV measurements with AM1.5G conditions.

#### 4.2.2 IV and CV Measurements

The IV characteristics of four different samples are shown in Figure 4.8. Sample A15S1 was fabricated with EDT (30 layers), whereas sample A16S5, A16S7 and A17S8 with BDT (12, 32 and 15 layers, respectively). Each of the measurements was performed right after taking the sample out of a glove box with an inert atmosphere. The extracted device parameters are given in Table 4.6.

Device	$J_{sc}$ [mA/cm <sup>2</sup> ]	$V_{oc}$ [V]	FF [%]	PCE [%]	$C_0$ [nF]	$W_{afm}$ [nm]	$W_{cap}$ [nm]
A15S1 dev7	6.14	0.403	0.45	1.1	2.53	-	72
A16S5 dev4	4.31	0.588	0.36	0.94	1.17	151.2	156
A16S7 dev9	1.41	0.604	0.33	0.29	0.45	403.6	401
A17S8 dev6	9.82	0.451	0.55	2.46	5.08	-	35

Table 4.6: Extracted device parameters of four different solar cells, i.e. A15S1, A16S5, A16S7 and A17S8, respectively.

The cells exhibit clear rectification characteristics and a stable behaviour in air during the experiment. The highest current densities in dark and light measurements were found for the A17S8-BDT solar cell, which results in a higher short-circuit current  $J_{sc}$ . The efficiency is the highest for this cell and is 2.46%. The measured values of the best cell are comparable to what was measured in previous works [2, 3, 10].

The corresponding CV characteristics of the same samples are depicted in Figure 4.9. Other than expected from previous work in Refs. [8, 11], no voltage dependence of the capacitance can be encountered for A15S1, A16S5 and A16S7, whereas A17S8 showed a minimal change. This means, that either the measurement frequency of 100 kHz is too high for that case or the film is fully depleted even when no voltage is applied. In Section 4.2.5 it is explained why the first case is true.

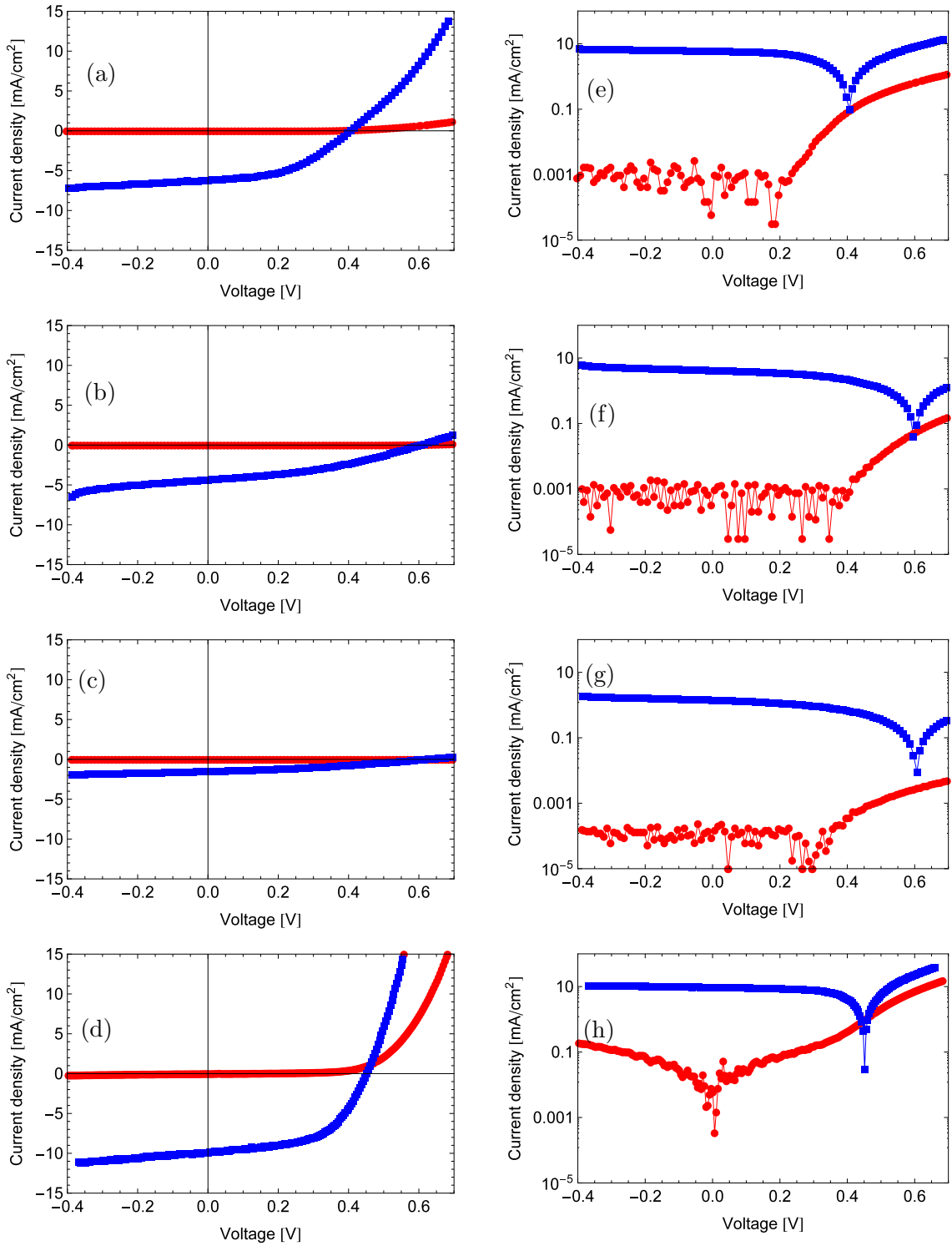


Figure 4.8: Dark and light IV characteristics. The linear curves are given in (a-d) for A15S1dev1, A16S5dev7, A16S7dev9 and A17S8dev6, respectively. The corresponding logarithmic curves are shown in (e-h).

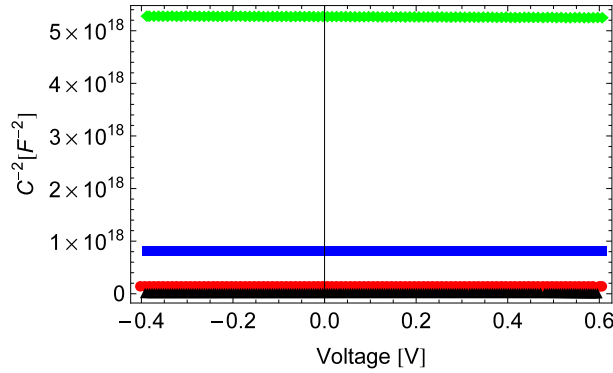


Figure 4.9: CV characteristics for A15S1dev1(red), A16S5dev7(blue), A16S7dev9(green) and A17S8dev6(black), respectively.

However, from the capacitance, the film thickness was calculated according to Equation 3.6, i.e.  $W_{\text{cap}} = \frac{\epsilon A}{C}$ . For sample A16S5 and A16S7, a comparison was made with atomic force microscope (AFM) measurements resulted in layer thicknesses of 12.6 nm for the two samples and its production method. The values are given in Table 4.6 for both and are in good agreement with each other.

#### 4.2.3 Degradation Measurements in Dark

To test the stability and the degradation of the fabricated solar cells in ambient air, IV-curves were acquired over a week. For the three solar cells from last section, Figure 4.10 shows their behavior in the dark. The main degradation happens in the forward bias characteristic as indicated in Figure 4.10(a-c). Figure 4.10(d-f) indicates the difference of two subsequent IV curves calculated according to the following equation:

$$\text{RMSError}[\text{day}_i] = \|\text{IVCurve}[\text{day}_{i+1}] - \text{IVCurve}[\text{day}_i]\| \quad (4.1)$$

After the third day, the curve of sample A15S1 was stabilized, whereas for sample A16S5 a minimal change was observed. By day three, the characteristic transformed from a diode to a high ohmic resistor. This effect could be due to oxidation processes as reported by Ref. [8]. The curves for A16S7 had the same evolution as for A15S1, but the current density is so small that almost nothing happened over the week in comparison to the other two samples.

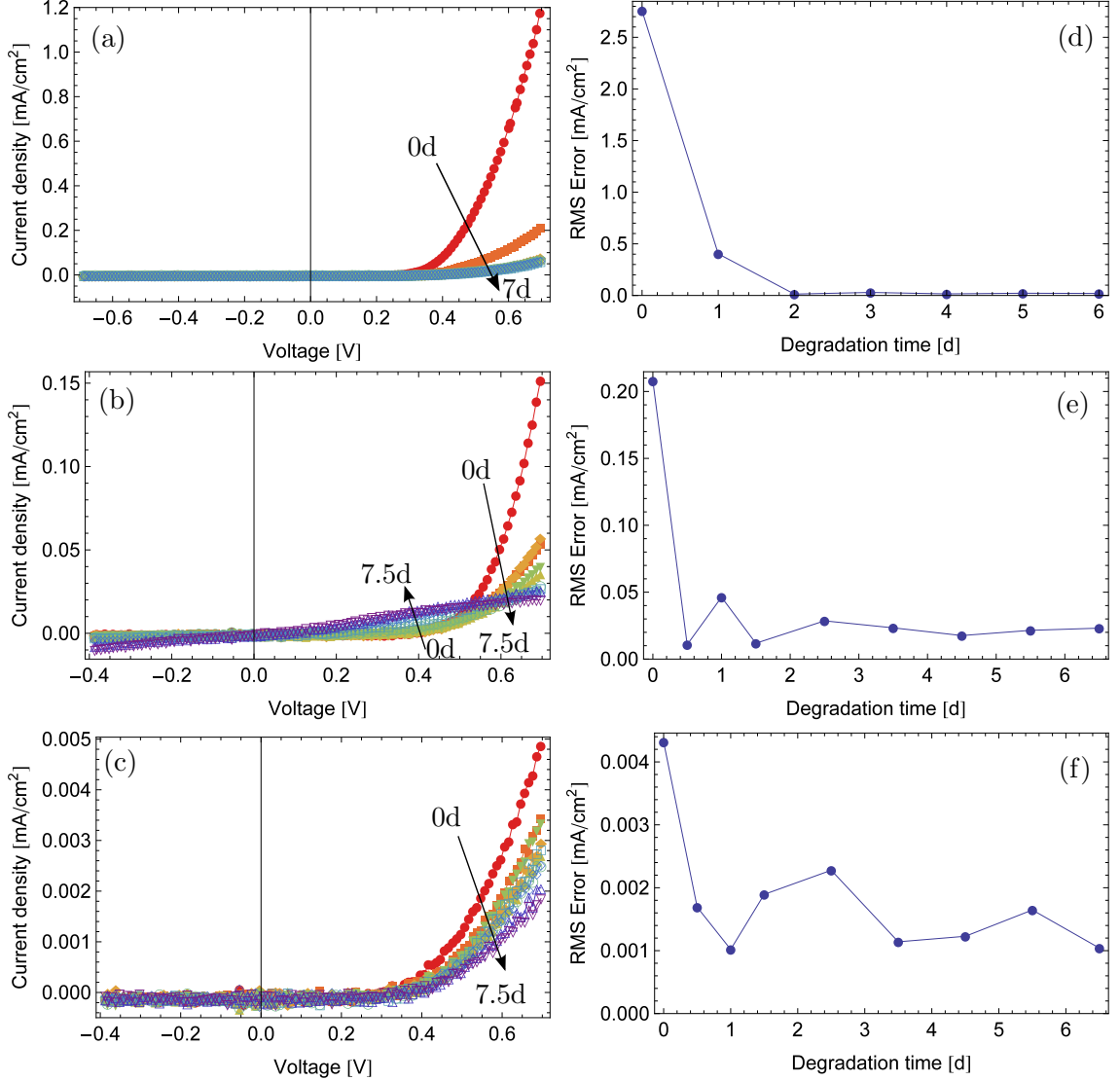


Figure 4.10: Degradation measurements under dark conditions. The evolution of the IV-curves measured over a week are given for sample A15S1,A16S5 and A16S7 in Figure (a),(b) and (c), respectively. Figure(d),(e) and (f) indicate the RMS value between two following curves.

#### 4.2.4 Degradation Measurements in Light

Sample A16S5 and A16S7 were additionally tested under illumination. The IV-degradation over a week is depicted in Figure 4.11(a)(b). The obtained values for open-circuit voltage  $V_{oc}$ , short-circuit current  $J_{sc}$ , fill factor  $FF$  and power conversion efficiency  $PCE$ , normalized to the initial value are shown in Figure 4.11(c)(d). For both samples, the open-circuit voltage remained almost constant, whereas the other three parameters strongly decreased with time.

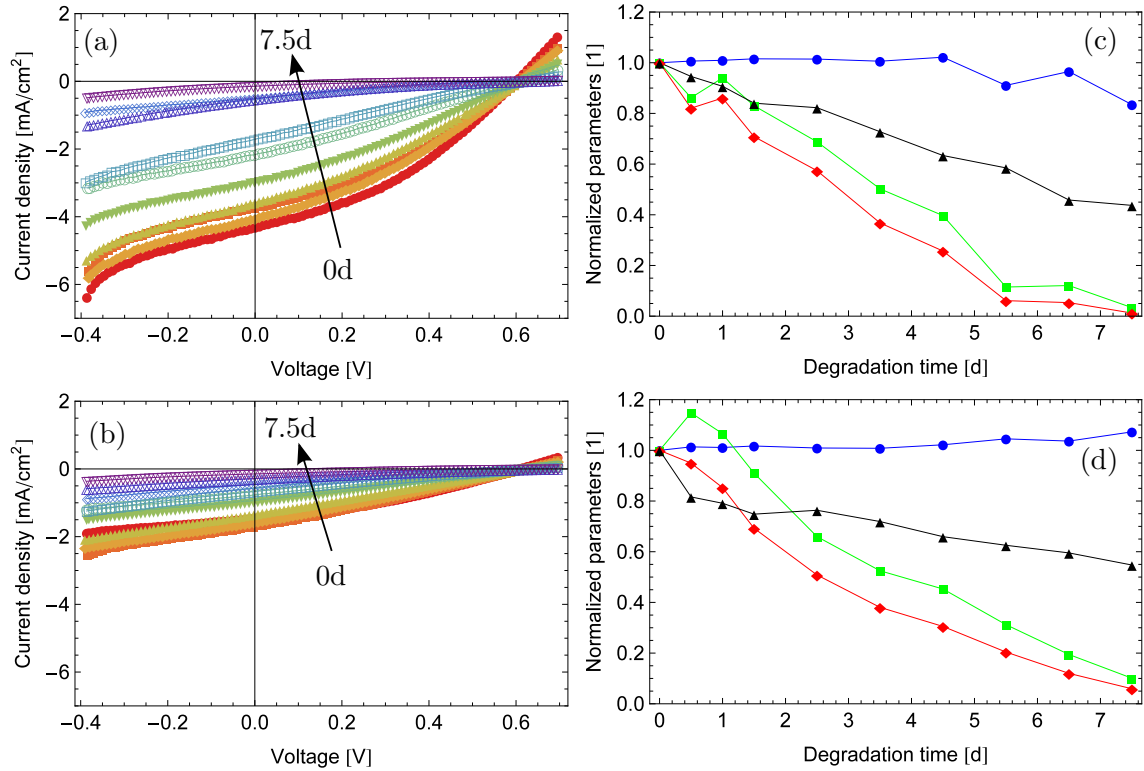


Figure 4.11: Degradation measurements under illumination (AM1.5) conditions. The evolutions of the IV-curves are shown in Figure(a) for sample A16S5 and (b) for sample A16S7, respectively. The evolution of the corresponding open-circuit voltage (blue), short-circuit current (green), fill factor (black) and power conversion efficiency (red) are given in Figure (c) for sample A16S5 and (d) for sample A16S7, respectively.

#### 4.2.5 Impedance Spectroscopy

In previous CV measurements explained in Section 4.2.2 it was observed, that the samples showed no voltage capacitance dependence, i.e. the same capacitance was measured for all applied voltages.

In a previous work [12], Clifford et al. showed the possibility to measure a such dependence by applying a measurement signal with a small frequency, i.e. 20 Hz. As a consequence, an impedance spectroscopy measurement was performed, where the frequency of the applied signal is varied over several order of magnitudes. The resultant capacitance at each measured frequency is shown in Figure 4.12. A voltage-capacitance dependence can be recognized in the range from 0.1 to about 500 Hz. At higher frequencies the capacitance changes no longer for different voltages.

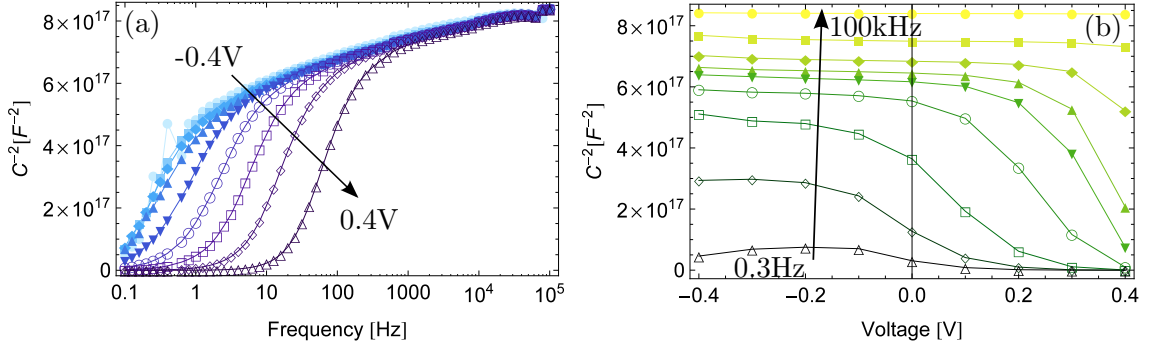


Figure 4.12: Impedance spectroscopy. The inverse squared capacitance at different frequencies for voltages between -0.4 V and 0.4 V are given in (a). The voltage dependent capacitance for different frequencies is depicted in (b).

#### 4.2.6 Mott-Schottky Analysis

The data presented in Figure 4.12(b) is a so-called Mott-Schottky (MS) plot. Its slope  $m$  reveals the free carrier concentration  $N$  according to the following equation:

$$m := \frac{d}{dV} \frac{1}{C^2} = \frac{2}{A^2 e \epsilon N}, \quad (4.2)$$

where  $A$  is the device area,  $e$  the elementary charge and  $\epsilon$  the effective permittivity of the material. Additionally, the intercept of the line with the voltage axis lead directly to the built-in voltage  $V_{bi}$  [8].

This model reveal only reliable parameters when the sufficiently large capacitance changes are observable. There exists two limitations:

- Spatial limitation: When the semiconductor film is too thin, the depletion width cannot be changed and therefore no capacitance change is possible.
- Velocity limitation: When the signal frequency is too high, charge carriers cannot be brought near the depletion edge, where they could contribute to a change of the depletion width and the capacitance, respectively. Only the geometric capacitance is then observable.

Some of the curves in Figure 4.12(b) exhibit a drop off in  $\frac{1}{C^2}$  with voltage. In Figure 4.13(a) there curves are replotted and fitted by two lines before (blue) and after (red) the drop off. The blue lines are nearly flat indicating a minimal capacitance change and a voltage region where the two mentioned limitations occur. The capacitance values of the blue lines are around 1.3 nF, which corresponds to a depletion width of 145 nm. Since the film thickness of this sample (A15S4) was estimated to be 150 nm, only a minimal change of the depletion width and the capacitance is possible. Therefore we applied the MS analysis only to the red lines.

The corresponding carrier concentrations are shown in Figure 4.13(b). The carrier concentrations are between  $1.2 \cdot 10^{16} \text{ cm}^{-3}$  and  $4 \cdot 10^{16} \text{ cm}^{-3}$  up to 200 Hz.

The corresponding values of the built-in voltage are depicted in 4.13(c) and are in reasonable range between 0.2 V and 0.5 V up to 100 Hz and increase then beyond 2 V.

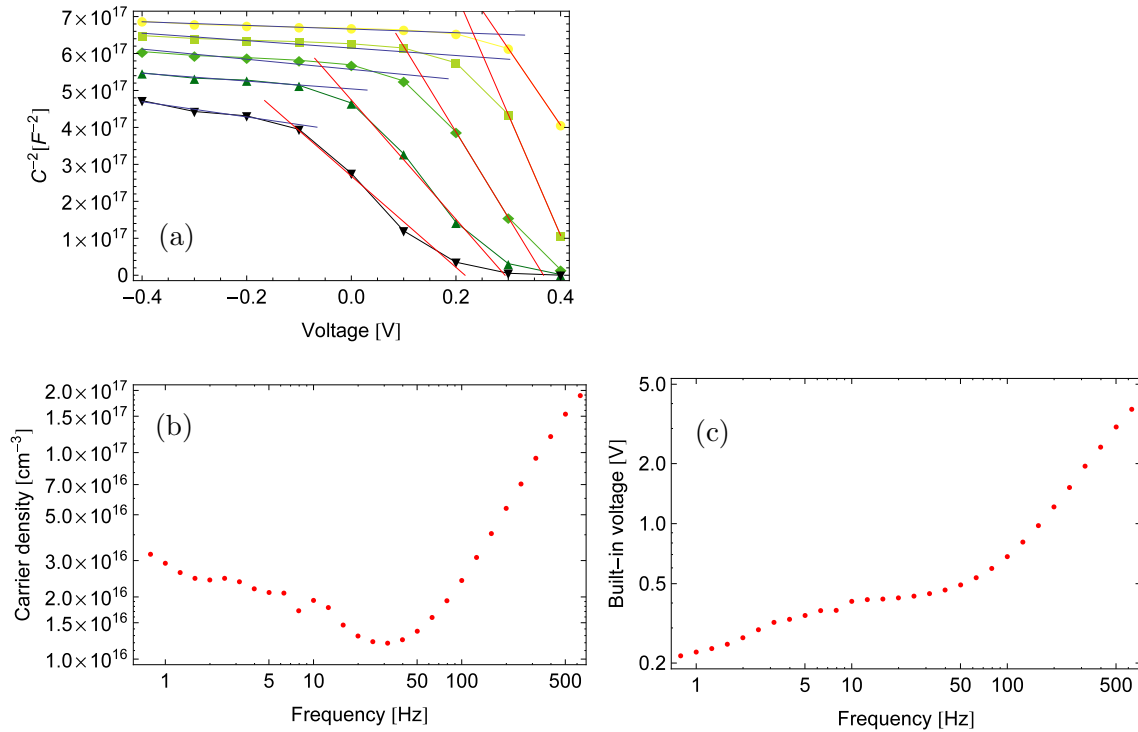


Figure 4.13: Mott-schottky analysis on impedance spectroscopy data. Two line fit model through data of Figure 4.13(a) is indicated in (a). The corresponding carrier densities and built-in voltages for the red curves are depicted in (b) and (c), respectively.

#### 4.2.7 Summary and Conclusions

The device characterization performed during this thesis lead to the following results and conclusions:

- Several samples were successfully fabricated and characterized as solar cells by investigating their IV curves. They showed all rectification behaviour due to the its diode structure. In the best case, a power conversion efficiency of 2.46% was measured.
- Degradation measurements over a week showed that the dark IV curves saturate after about 3 days. In the illuminated case, large reductions of power conversion efficiency, fill factor, and the short-circuit current were observed, whereas the open-circuit voltage stayed almost constant.

Degradation should therefore be controlled or taken into account in the explanations of the electronic spectroscopy data.

- CV measurements and impedance spectroscopy showed that for low measurement frequencies (i.e. below 100 Hz) a voltage capacitance dependence could be observed.

- From a Mott-Schottky analysis of CV data, two regions were found. For forward voltages and frequencies below 100 Hz, a linear fit lead to reliable values for carrier concentrations around  $10^{16} \text{ cm}^{-3}$  and built-in voltages between 0.12 V and 0.4 V. For reverse voltages, the linear model is not applicable.

# Chapter 5

## Development of a Setup for DLTS Measurements on QD Solar Cells

In this Chapter the current DLTS measurement setup we developed and used for trap investigation is presented. In Section 5.2 the hardware components are discussed. The connections and specifications of each component can be found in Appendix C. The software of the setup is discussed in Section 5.3 with respect to the data acquisition and digitized data processing, respectively. Finally, the characterisation performed of the setup is given in Section 5.4.

### 5.1 Capacitance vs. Current DLTS

Initially our idea was to have a DLTS setup able to acquire both capacitance and current transients. In this initial setup, a Boonton 72ad capacitance bridge was embedded and tested. Since the Boonton 72ad (and also other capacitance meters available) measures the capacitance at a fixed frequency of 1 MHz, it was impossible to see transients based on the space charge capacity according to the observations explained in Section 4.2.5. Therefore, the only transient sensing unit in the setup is a transimpedance current amplifier. The DLTS setup with integrated capacitance meter can be found in Appendix C.

### 5.2 Hardware Configuration of the Setup

The setup for current DLTS measurements is shown in Figure 5.1 as it is in the laboratory. For a clearer view, two additional enlargements are shown of the devices located on a ceiling table and of the devices on an optical measurement table, respectively. A block diagram of the setup is depicted in Figure 5.2. It contains all important electronic components and external connections. In the following, the tasks of the devices within the system are explained one by one.

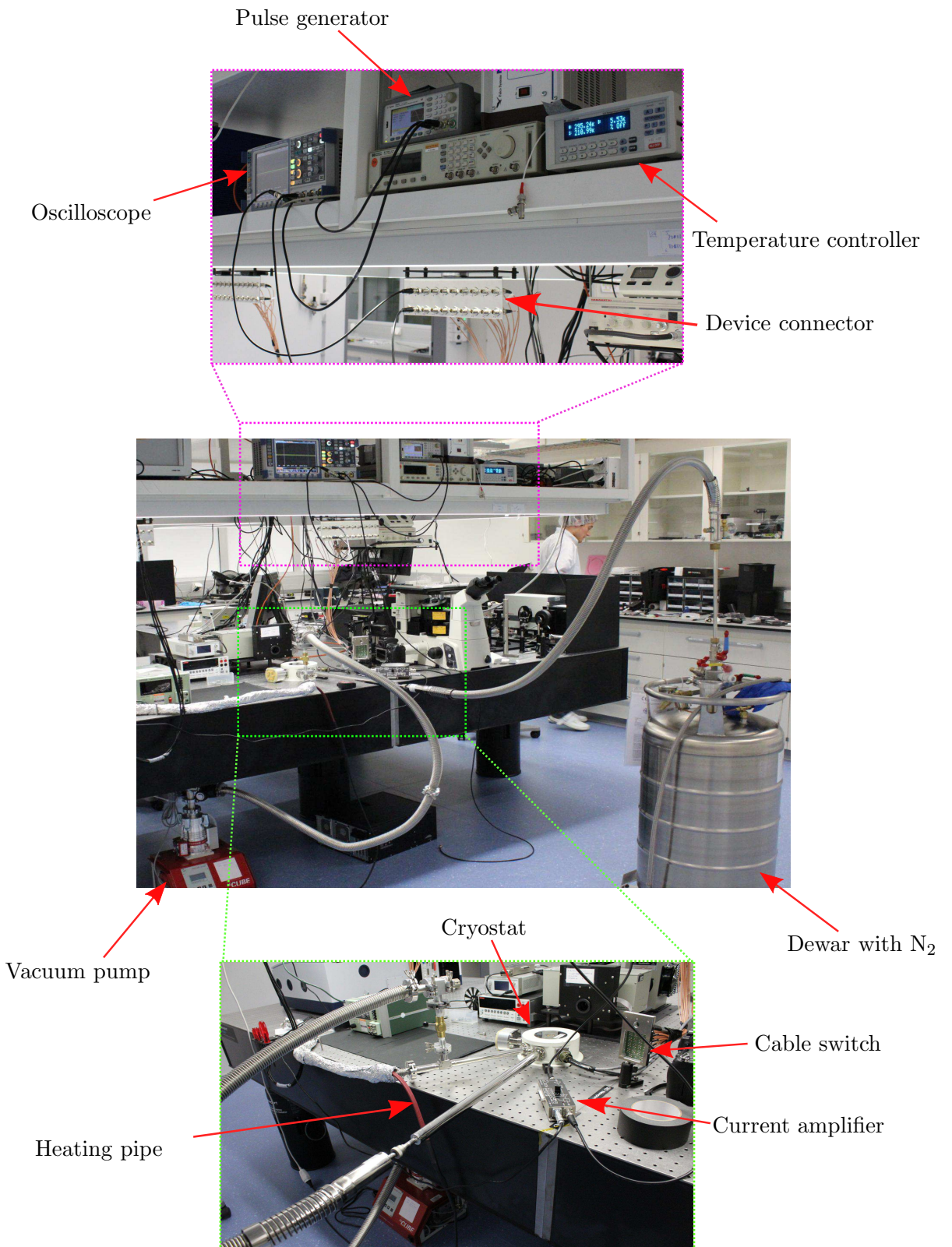


Figure 5.1: Current DLTS setup in the laboratory. Oscilloscope, pulse generator and temperature controller are located on a ceiling table (showed in detail in pink dotted line). The cryostat and current amplifier are on the optical measurement table (designated by the green dotted line). The dewar filled with liquid  $N_2$  and the vacuum pump stand on the floor.

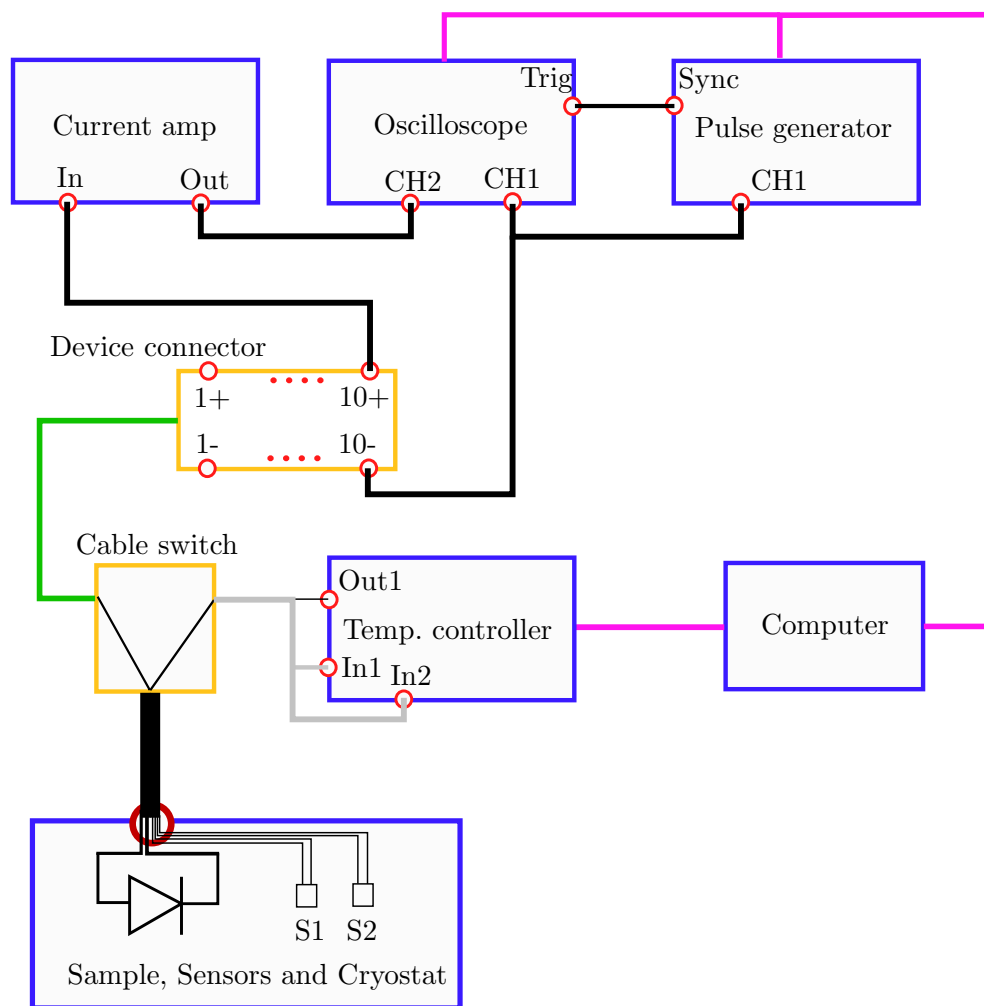


Figure 5.2: Schematic of the current DLTS setup. The devices are depicted in blue and the cable connectors in yellow. Broad black lines indicate coax cables, pink lines represent USB-cables. Red circles signify connectors right at devices rack.

**Pulse generator**

In this thesis, an AGILENT 33522 arbitrary waveform generator (AWG) is used for the purpose of applying periodically pulses to the sample. The minimum pulse width is 16 ns and the pulse amplitude can be adjusted between 1 mV and 10 V. Its sync output is used to trigger the oscilloscope externally.

**Current amplifier**

We measure low current transients using a FEMTO DHCRA transimpedance amplifier (TIA). The current is converted with an amplifier stage, ranging from  $10^2$ – $10^8$  V/A, into a voltage acquired by the oscilloscope. During the thesis, the two ranges  $10^4$  and  $10^5$  V/A were used together with the high speed setting to ensure the highest sensitive range and no overload conditions under zero bias. Additionally, we used a bandwidth of 1 MHz for the integrated low pass filter.

**Temperature controlling**

To measure transients at various temperatures a Janis ST-500 cryostat is used. The cryostat is equipped with a sample holder, a heater and two temperature sensors. Cooling is enabled by liquid nitrogen stored in a dewar and flowing continuously through the cryostat. Heating is carried out against the cooling, while the temperature controlled by a Lakeshore 335 temperature controller.

**Oscilloscope**

A Rhode & Schwarz RTM 1054 oscilloscope is used to record the signal of the transimpedance amplifier and the pulse generator. The oscilloscope offers the option to smooth the signal by taking the average over many waveform repetitions.

**Personal computer**

The overall controlling and monitoring of the setup in the laboratory is performed by a personal computer. The integrated automatization software LabVIEW enables the setting of the individual instruments, whereas the cheapness of memory allows the storage of huge amount of data.

## 5.3 Software of the Setup

The software written for the setup is divided into two main parts:

- LabVIEW part for the analogue data acquisition while measuring in the laboratory (Section 5.3.1)
- Mathematica part for the data processing after measured data is available (Section 5.3.2)

### 5.3.1 Software for Data Acquisition

To record data with the setup stated above, several virtual instruments were developed and integrated into an existing LabVIEW framework called *Nsweep*. These instruments allow control of the real instruments and are explained in the following.

### Transient measurement instrument

This virtual instrument enables the transient measuring procedure described in Section 3.4.1 and builds a subsystem of the DLTS setup, where transient signals are acquired by applying voltage pulses at a constant temperature.

Figure 5.3(a) indicates the applied signal and the corresponding measurement parameters, which are summarized in Table 5.1. The voltage signal is defined by four parameters: the fixed forward  $V_F$  and reverse voltage  $V_R$ , respectively, the pulse width  $t_{\text{width}}$  and the time between two successive pulses, i.e. the period  $T$ . The resultant transient as shown in Figure 5.3(b) is acquired from the time point  $t_{\text{acq,start}}$  during a time  $t_{\text{acq}}$ . The corresponding LabVIEW interface is depicted in Figure 5.4 and contains all mentioned parameters. When this instrument is used, the enable button in the upper left corner has to be pressed. To set additional parameters of the devices involved, a selection button in the upper right corner was introduced. Its functionality and the corresponding parameters are explained in Appendix D.

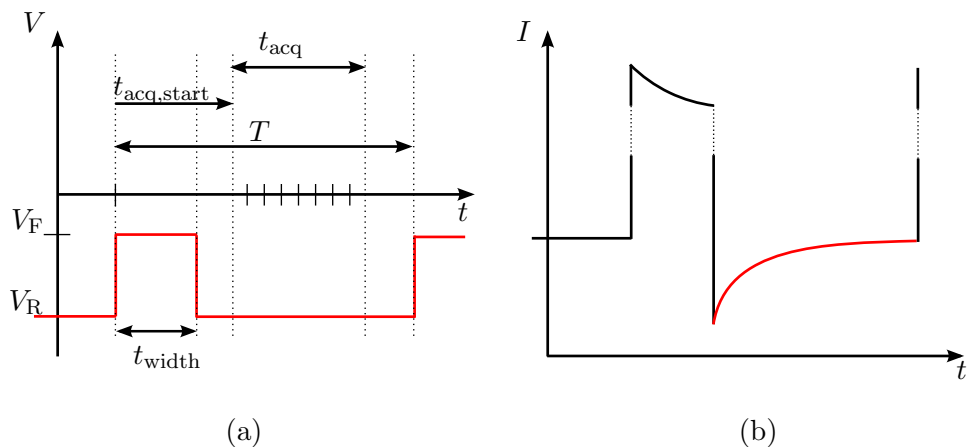


Figure 5.3: Timing diagrams of single transient operation mode. The pulse applied to the sample is shown in (a) with the corresponding measurement parameters. The output as a single transient is indicated in (b).

Single transient settings		
Parameter	Description	Remark
$V_F$	Forward voltage or pulse height [V]	Absolute
$V_R$	Reverse voltage or baseline [V]	Absolute
$t_{\text{width}}$	Pulse width [s]	-
$T$	Period [s]	-
$t_{\text{acq,start}}$	Start acquisition time [s]	Measured from pulse begin
$t_{\text{acq}}$	Acquisition time [s]	Length of acquisition
$N_{\text{avg}}$	Number of averages [1]	Average done by oscilloscope

Table 5.1: Single transient settings for LabVIEW program.

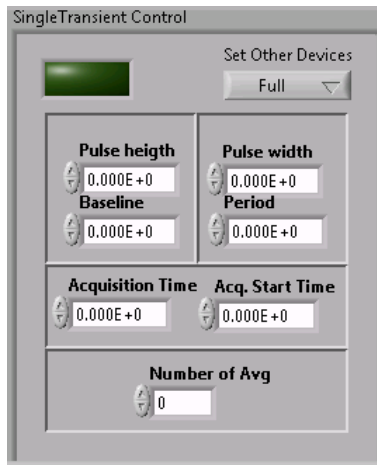


Figure 5.4: LabVIEW single transient interface.

### Voltage sweep

For the purpose to observe transients for different reverse voltages applied to the sample, a voltage sweep was implemented. Thereby all parameters of the previous instrument are carried over, except the reverse voltage  $V_R$ . This voltage is set step wise from a start value  $V_i$  towards and end value  $V_f$ . The corresponding measurement parameters are given in Table 5.2, whereas the LabVIEW interface is given in Appendix D.

Voltage sweep parameters	
Parameter	Description
$V_i$	Initial reverse voltage [V]
$V_f$	Final reverse voltage [V]
$N_{step}$	Number of steps between $V_i$ and $V_f$ [1]

Table 5.2: Voltage sweep parameters in the LabVIEW framework.

### Temperature setting instrument

Single temperature setting mode is used to set a distinct temperature around the test device. Figure 5.5(a) shows the corresponding timing diagram with the measurement parameters. The process starts at  $t_0$  by ramping the temperature up or down towards the setpoint with a desired ramp rate. Around this point a stability margin is set where temperature variations are allowed (indicated in blue). When entering this region, it is checked if the temperature is stable in a time window  $t_{sw}$ . When the temperature goes beyond the margin (see violet box), a new time window (green box) starts at that point and temperature is checked again for the same time window. If it was stable in a time window and an overall timeout was not exceeded (yellow box), a measurement can take place. The corresponding LabVIEW interface is depicted in Figure 5.6. It contains the measurement parameters explained above and some additional settings. They are summarized in Table 5.3.

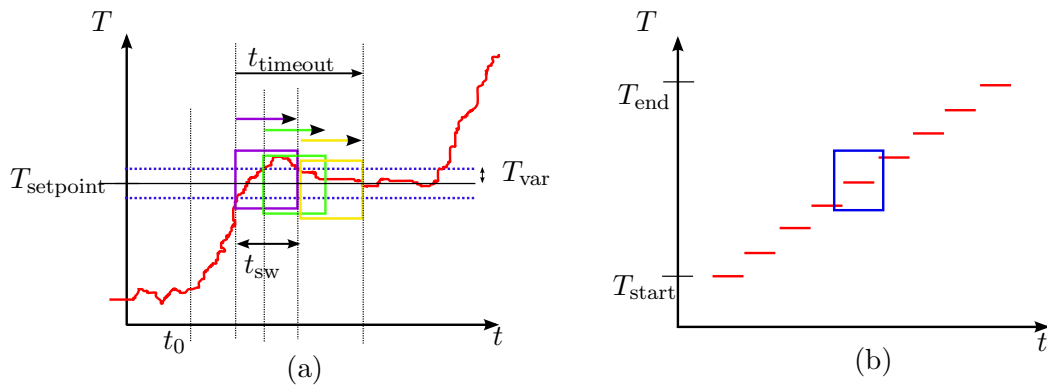


Figure 5.5: Timing diagrams of temperature setting. Single temperature mode is indicated in (a), while the temperature sweep sequence is indicated in (b).

Single temperature settings		
Parameter	Description	Remark
$T_{\text{setpoint}}$	Desired temperature point [K]	-
Ramp Rate	Temperature change per minute [K/min]	-
$T_{\text{var}}$	Variation of temperature while stabilizing [K]	Measured from setpoint
$t_{\text{sw}}$	Length of stability window [s]	-
$t_{\text{timeout}}$	Overall timeout [s]	-
Heater Output	Index of used heater	1 was taken
Heater Range	Heater ranges (Off, low, medium, high)	High was taken
Gain (P)	P element of PID controller	-
Reset (I)	I element of PID controller	-
Rate (D)	D element of PID controller	-

Table 5.3: Single transient settings for LabVIEW program.

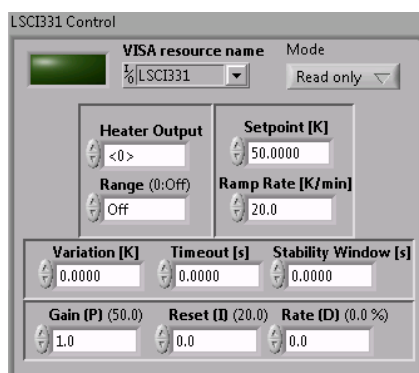


Figure 5.6: LabVIEW single temperature interface.

Additionally, the instrument can run in three modes:

- Read only: Temperature is only read. No temperature control is performed.
- Set and Read: Temperature is first set according to the process described above and than read.
- Set only: Temperature is only ramped to the setpoint.

### Temperature sweep

The temperature sweep is used in combination with the single transient mode to obtain transients at several temperatures. It uses all parameters from the previous explained instrument, except for the set point, which is set step wise from a start value  $T_{\text{start}}$  towards and end value  $T_{\text{end}}$ . This is depicted in Figure 5.5(b). The three measurement parameters are given in Table 5.4, whereas the LabVIEW sub block is given in Appendix D.

Sweep temperature parameters	
Parameter	Description
$T_{\text{start}}$	Initial temperature [K]
$T_{\text{end}}$	Final temperature [K]
$N_{\text{step}}$	Number of steps between $T_{\text{start}}$ and $T_{\text{end}}$ [1]

Table 5.4: Sweep temperature parameters in the LabVIEW framework

### Data storage

For data processing, the LabVIEW framework stores the signals measured from the oscilloscope, i.e. the pulse signal and the current transient, together with primary settings into a .txt file. Each single measurement and each step from a sweep is saved as a line, which has the following entries from left to right:

- (1) Time stamp [s], (2) Sweep parameter [K], (3) Temperatures from both sensors [K], (4) Baseline of the pulse [s], (5) Pulse height [s], (6) Pulse width [s], (7) Period [s], (8) Acquisition time [s], (9) Acquisition start time [s], (10) Average number [1], (11) Pulse data points [V], (12) Transient data points [V]

### 5.3.2 Software for Data Processing

To analyse the measured data, five main algorithms were implemented in Mathematica:

- Conventional Boxcar approach
- Gaussian Boxcar approach
- Exponential approach
- Fourier approach
- Direct fitting approach

The mathematical treatment is given in Chapter 3.5. In general, they are all embedded into a separate Mathematica notebook and have a similar structure with respect to the data flow depicted in Figure 5.7. Most important steps and functions, which are labelled in type writer font, are explained in the following.

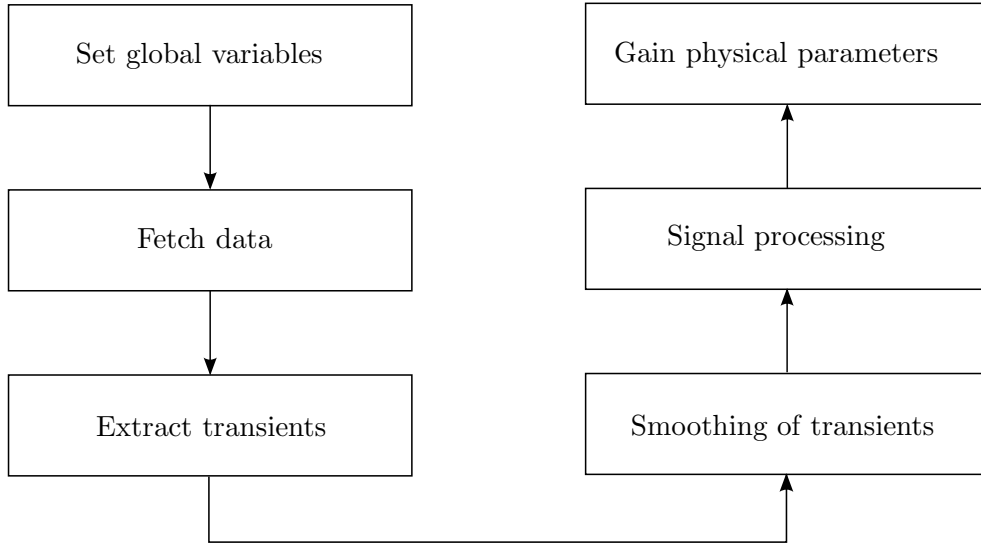


Figure 5.7: Data flow graph of data processing

First, global variables (like data path, amplifier gain, etc.) are set and declared. Afterwards, the measured data as well as the settings described in Section 5.3.1 are read in (`LoadData`) and stored into the corresponding variables. In a next section, the desired transients (either capture or emission transients) are extracted from the data (`ExtractTransientsFromData`) after the overload time of the amplifier has been set. The overload time defines the time, where data points are truncated for further processing.

Since erroneous data can emerge during the transfer from the oscilloscope to the PC, a median filter (`MedianFilterMJ`) was introduced, which also filters noisy signal parts. For the case when only noise is present, a low-pass filter (`LowPassFilter`) of the first order was developed.

With the smoothed transients, signal processing with one of the above explained DLTS algorithms (`ConventionalBoxCarMethod`, `GaussianBoxCarMethod`, `FourierMethod` or `ExponentialMethodMapping`) can be performed following these steps:

1. Choice of the weighting function  $w(t)$  according to Equation 3.12, 3.16, 3.18 or 3.19.
2. Correlation according to Equation 3.11 (`CorrelationFilter`)
3. Computation of the time constants and the corresponding temperatures

The last step is different for the Fourier approach and the three others. In the Fourier approach the time constants are calculated directly by building the quotient of the Fourier coefficients according to Equation 3.20. The corresponding temperature values are equal to temperatures from the measured transients.

For the conventional Boxcar approach, time constants are extracted according to Equation 3.15 (`FindTauMaxForConventionalApproach`). For the Gaussian Boxcar approach

and the exponential approach, Equation 3.11 can be written as

$$S = \frac{1}{P} \int_0^P \frac{A}{\tau_e} \exp(-t/\tau_e) (\exp(-(t-t_1)^2/2\sigma^2) - \exp(-(t-t_2)^2/2\sigma^2)) dt \quad (5.1)$$

and

$$S = \int_{\tau_H}^{\tau_m} \frac{k}{\tau_e} \exp(-t/\tau_e) \exp(-t/\tau_r) dt, \quad (5.2)$$

respectively, where

$$I(t) = \frac{k}{\tau_e} \exp(-t/\tau_e) \quad (5.3)$$

was inserted.

Time constants are extracted by calculating the maximum of  $S$  with respect to  $\tau_e$  ([FindTauMaxForGaussianApproach](#), [FindTauMaxForExponentialApproach](#)).

For all three algorithms, the temperature is obtained from the maxima of the DLTS spectra. Since the spectra are usually noisy around the maxima, a polynomial fit of order 2 is applied around the highest values ([FindDataAroundMax](#)).

Time constants can also be acquired by fitting the transients, with an adequate model. In the direct fitting approach, a single exponential decay is assumed as given in Equation 5.3 ([FindExponentialFit](#)).

The extracted parameters can then be used to obtain the physical parameters, i.e the activation energy ([FindEnergy](#)), and a graphical representation as explained in Section 3.3.

## 5.4 Characterization of the Setup

Prior to use, the components of the setup were tested as explained in the following.

### 5.4.1 Current Measurements with Transimpedance Amplifier (TIA)

The transimpedance characteristic of the TIA was first tested with the commercially available silicon diode 1N5817. In doing so, the ModuLab SMU applied a voltage and measured the current flowing through the diode. At the same time, the current was sensed by the TIA, whereas its voltage output was acquired by ModuLab, too. The two curves are identical as shown in Figure 5.8, when current values measured from TIA were divided by a factor of 2. This factor was also observed by applying different voltages to a 10 kΩ resistor and measuring the current with the DLTS setup.

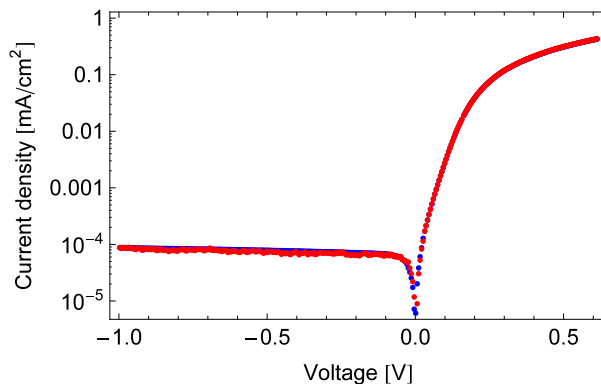


Figure 5.8: IV test with transimpedance amplifier. Two IV curves measured directly by ModuLab (red) and together with a transimpedance amplifier (blue) are identical.

#### 5.4.2 Noise Reduction Considerations

After checking the amplifiers functionality, its noise level was characterized within the setup. Therefore, oscilloscope was first connected only to the amplifier and whereas the settings are the following:

- Gain:  $10^4$  V/A at High speed mode
- Cut off frequency: 1 MHz
- Coupling: DC

The measured RMS-noise was measured at 26 nA. The amplifier was then attached to the cryostat (no sample mounted!) with the sample connector and cable switch. It was observed that the sample connector should electrically be connected to the metal plate of the table, reducing its noise level significantly. In this configuration, the noise raised towards 140 nA. The RMS-noise with mounted sample in the cryostat and attached source (pulse generator) raised further towards 3.5  $\mu$ A. Putting the cover on the cryostat, reduced the noise level to 1.5  $\mu$ A.

In a next step, the metal housing of the cryostat was electrically connected to the metal plate with tin foil of the optical table, thereby reducing the noise again to 1  $\mu$ A. In the cryostat, a connection was soldered between ground contact of the pin connection board and the housing itself. The final RMS noise for the configuration with source, lid, tin foil was measured at 600 nA.

#### 5.4.3 Temperature Sensor Calibration

Initially, the cryostat used in this thesis was equipped with one temperature sensor attached on the foot (S1) of the sample holder. With a built-in program, the PID parameters of the controller summarized in Table 5.5 were obtained with the purpose to stabilize the temperature in a minimum time at a ramp rate of 8 K/min. With this settings the adjustment takes 3 minutes per ramp step. To measure the exact temperature of the sample, a second sensor (S2) was mounted into the cryostat to attach it directly at the surface of the glass substrate as shown in Figure 5.9. The margin between the glass window in the lid of the cryostat depicted in Figure 5.9(b) and the sensor is relatively

Gain (P)	Reset (I)	Rate (D)
73.1	11.8	100

Table 5.5: PID controller parameter.

small. To guarantee that no thermal leakage occurs at the edge of the lid, the sensor was pressed with Kapton Tape onto the surface.

The temperature controller has access on both sensors at a time. When reading out the temperatures below and above room temperature, it was observed that the two sensors showed different output range. While the range for S1 was measured from 120 to 413 K, it went from 241 to 338 K for S2.

The temperature controlling is maintained by using the PID settings from Table 5.5 applied to sensor S1. The output from sensor S2 increases or decreases slightly slower, but is used for the readout.

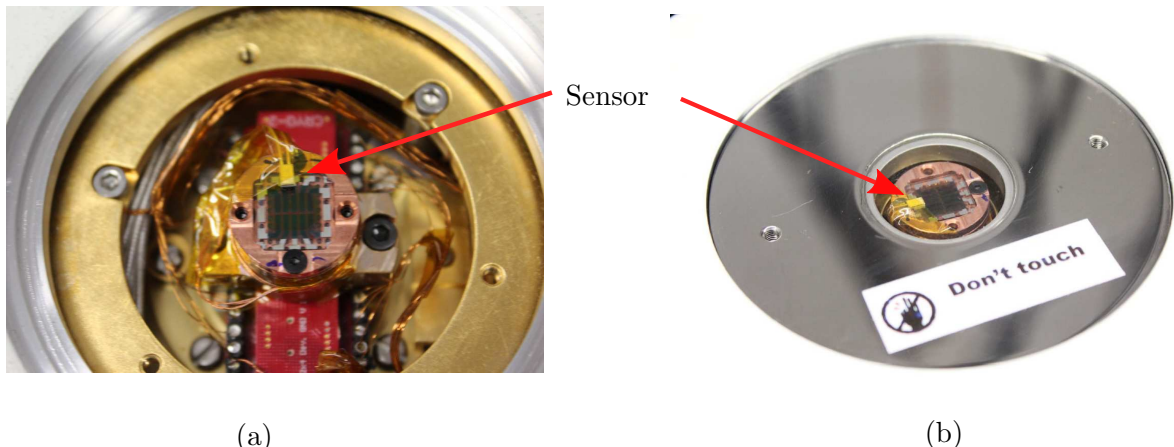


Figure 5.9: Cryostat with attached sensor on samples surface.

# Chapter 6

## Current Transient DLTS on PbS Solar Cells

In this chapter, DLTS measurements on colloidal solar cells and results are presented. In Section 6.1, a first DLTS measurements attempt is discussed together with the used parameters. A complete analysis on current transients is given in Section 6.2. The influence of temperature on IV curves is explained in Section 3, along with the DLTS analysis.

### 6.1 First Transients Measurements - Prove of Concept

In a first DLTS measurement, different situations and parameters were tested on a EDT sample (A15S1 dev1), which was already in ambient air for 2 months. The sample was cooled down to 77 K measured by sensor S1. Since no clear transient behaviour could be observed at a first glance, pulses on different time scales summarized in Table 6.2 were applied with a fixed reverse voltage at -0.7 V and a forward voltage of 0 V.

The output of the transimpedance amplifier (TIA) after the pulse voltage turned back to reverse conditions for the three settings is shown in Figure 6.1(a). At all three time scales no transient, but a displacement current could be observed. This current is due to charging and discharging of the geometrical capacitance when the electrical field changes and must be considered, since it can interfere with current transients that have to be analysed in a DLTS measurement. The longest delay can be observed for the longest applied pulse.

Afterwards, the reverse voltage was changed from -0.7 V to -0.1 V in steps of 0.1 V for the middle (red) time scale indicated in Figure 6.1(b). Here too, only a displacement current was observed. For the smallest applied voltage, i.e. -0.1 V, the TIA does not go into saturation.

Time scales of first experiment		
Pulse width [ms]	Period [ms]	Color in Figure 6.1
10	100	Blue
1	10	Red
0.1	1	Green

Table 6.1: Time scales used for the first experiment.

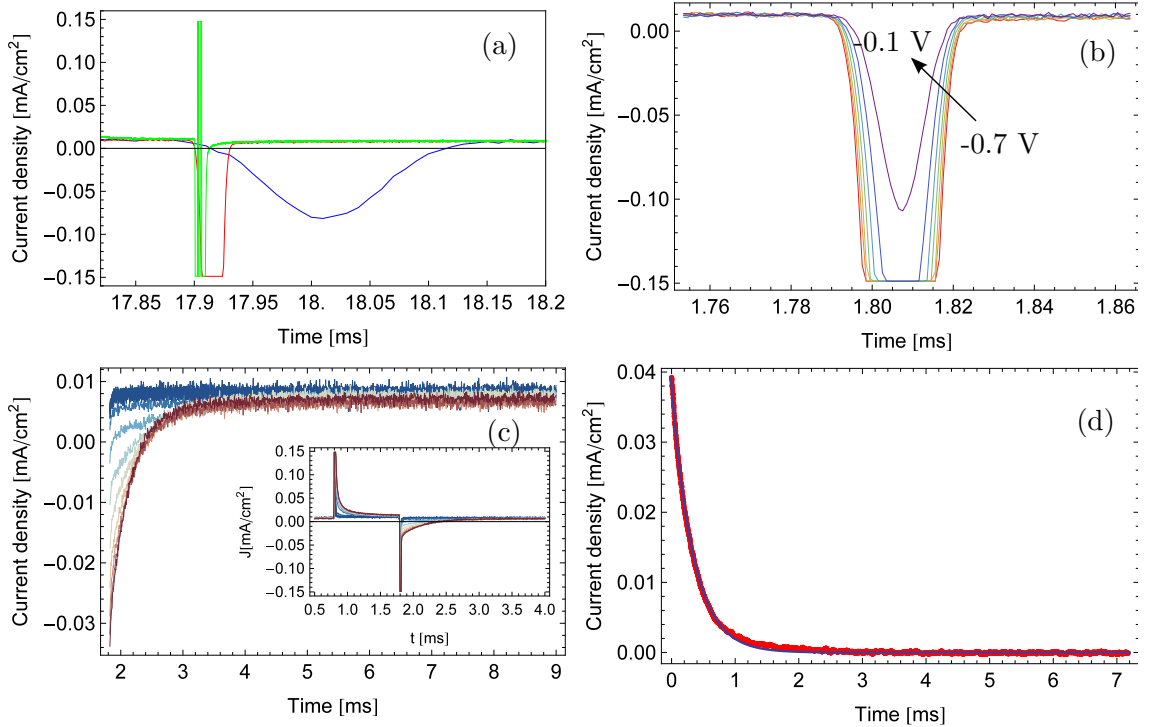


Figure 6.1: Several investigations in a DLTS experiment. The measured signal when pulses with different time scales (see Table 6.2) and when different reverse voltages are applied are shown in (a) and (b), respectively. First measured transients are given in (c). The exponential decaying form of one transient is illustrated in (d) with the corresponding fit (blue).

In a third attempt, the temperature was ramped up towards 300 K. A clear temperature dependent transient could be monitored as shown in Figure 6.1(c). Since the temperature was sensed not directly from the samples surface up to that point, no reliable temperature data was available. Nevertheless, the single transients were examined with respect to the shape. Figure 6.1(d) shows the inverted transient for 300 K. An exponential decay was confirmed with the fit indicated in blue. This transient has the smallest time constant of 0.35 ms that was measured during the experiment.

## 6.2 DLTS Analysis on Measured Current Transients

### 6.2.1 Description of the Experiment

In a second experiment, a BDT sample (A17S2) was investigated, which was stored in an inert atmosphere to minimize degradation. For this experiment and the following, the temperature was read out with the sensor mounted directly on the surface of the sample. The temperature was first ramped down to 119 K. By continuously applying trap filling voltage pulses to the sample, temperature was ramped up to 314 K, whereas every 4 K a current signal was recorded. Since transients could be observed in the first experiment, similar parameters were used and are summarized in Table 6.2.

Measurement parameters	
Parameter	Value
Pulse height	0 V
Baseline	-0.7 V
Pulse width	1 ms
Period	10 ms
Acquisition time	10 ms
Number of average	16
Temperature range	119 - 314 K
Ramp rate	8 K/min

Table 6.2: Measurement Parameters for Second Experiment.

In this experiment, temperature dependent current transients were measured and are shown in Figure 6.2(a). The data was filtered with a median filter according to Section 5.3.2. Below 242 K no clear transients could be observed, i.e. the measured signals are straight lines buried in the noise floor. Above 242 K, exponential decaying curves are visible.

By flipping the curves about the time axis and subtracting the current offset due to leakage as illustrated in Figure 6.2(b), a crossing of the transients is observable, which is due to the time constant dependence of the amplitude of the current transients (see Section 3.4.3).

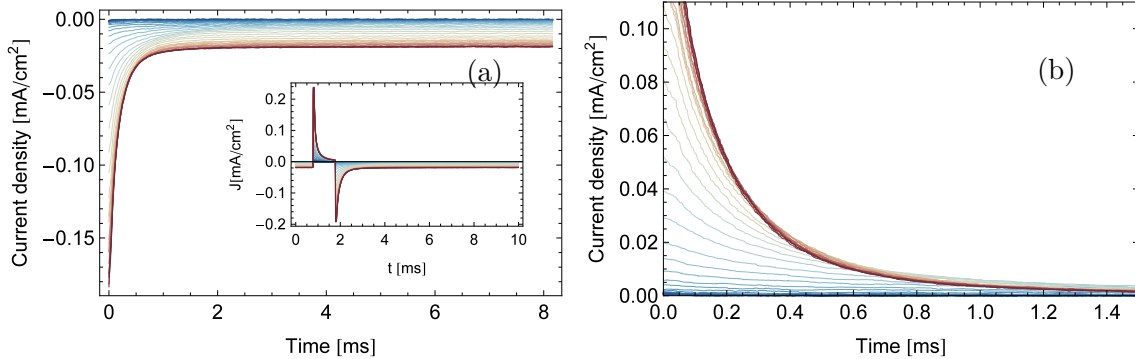


Figure 6.2: Measured current transients. The emission transients are depicted in (a). The inset shows the hole signal over a measurement period of 10 ms. Crossing of transients can be seen in (b).

### 6.2.2 Boxcar Approaches

A first analysis of the transients was done with the conventional and Gaussian Boxcar approach. First, the DLTS spectra were obtained by correlating the transients (see Section 3.5) and are indicated in Figure 6.3(a) for the conventional approach and in Figure 6.4(a) for the Gaussian approach, respectively. In both approaches, the spectra are noisy. Therefore, the temperature maxima were extracted by a polynomial fit of order 2 around the highest values of each spectrum curve illustrated by blue dots. Since no clear transients were observed below 250 K, the maxima lie all above that temperature and the spectra are flat for lower temperatures.

For the conventional approach, several ratios for the sampling times  $t_1$  and  $t_2$  were used. The Arrhenius data in Figure 6.3(b) is noisy for all ratios, but similar energies could be extracted as shown in 6.3(d). For the case of  $t_2/t_1 = 4$ , the Arrhenius plot and the extracted energy - 0.29 eV - together with the fitting line is given in Figure 6.3(c).

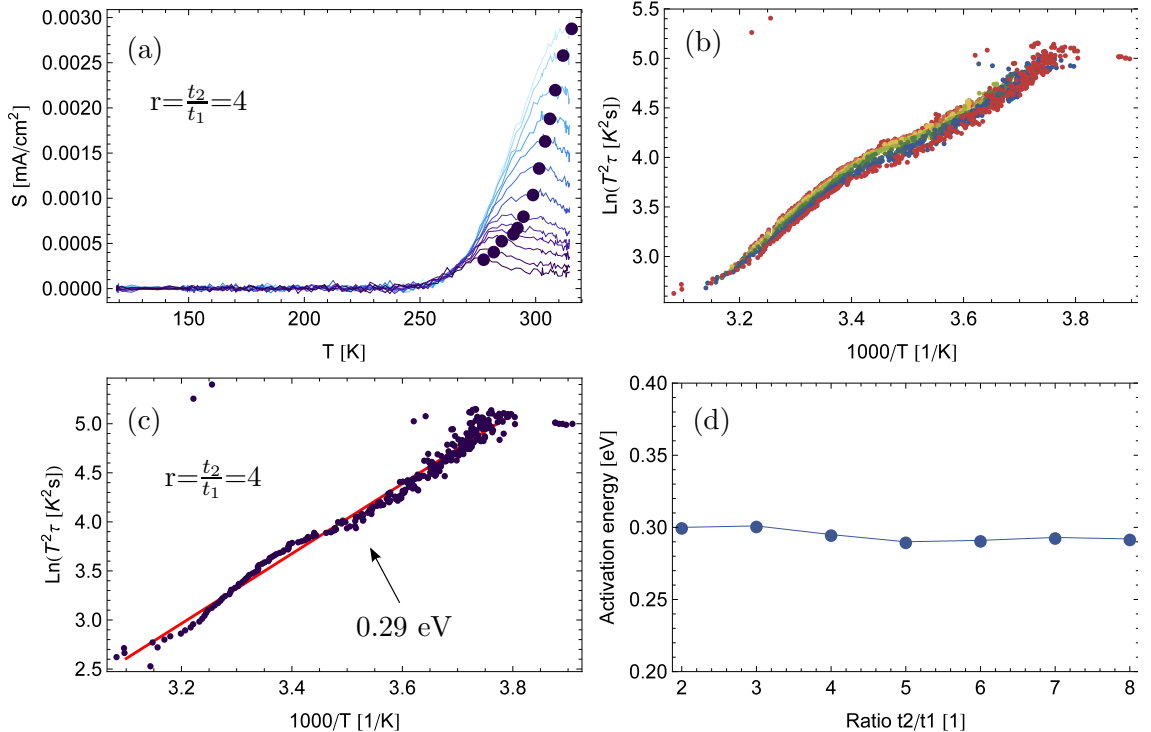


Figure 6.3: Results of conventional Boxcar approach. The DLTS spectra together with the maxima points are depicted in (a). The Arrhenius plot for  $r = 2 \dots 8$  are shown in (b), whereas for ratio equal to 4 is given in (c). All extracted energies are given in (d).

In the Gaussian approach a similar result can be expected as in the conventional approach, since the only degree of freedom that changes is the width of the sampling time, i.e. the standard deviation  $\sigma$  of a Gaussian shaped pulse (see Section 3.5.2). Several values for  $\sigma$  were tested. The respective Arrhenius data is illustrated in Figure 6.4(b), whereas the corresponding extracted energies are given in Figure 6.4(d). For the case of  $\sigma = 0.1$  ms and  $r = 4$ , the Arrhenius plot and the extracted energy - 0.29 eV - together with the fitting line is given in Figure 6.4(c). As opposed to the conventional approach, the Gaussian approach is less noisy at higher values of  $\sigma$  due to the filter effect of the Gaussian pulse form. However, both approaches show a slight deviation from a straight line, which is due to small errors when extracting the maxima in the DLTS spectra.

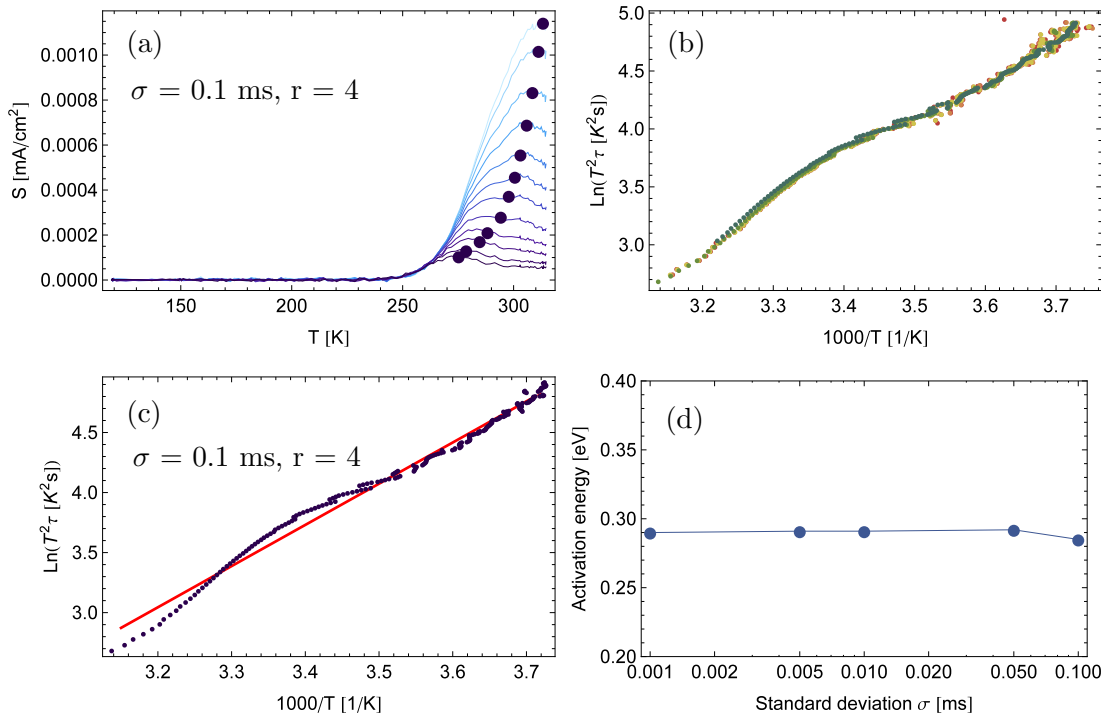


Figure 6.4: Results of Gaussian Boxcar approach. The DLTS spectra together with the maxima points are depicted in (a). The Arrhenius plot for  $\sigma$  (0.001, 0.005, 0.01, 0.05 and 0.1 ms) are shown in (b), whereas for  $\sigma$  equal to 0.1 ms is given in (c). All extracted energies are given in (d).

### 6.2.3 Fourier and Direct Fitting Approach

Additionally to the two Boxcar approaches discussed above, Fourier and a direct fitting approach were also used. Unlike in the former methods, time constants are gained by calculating the Fourier coefficients in the Fourier DLTS. Equation 3.20 for this purpose is given here again:

$$\tau_e(a_n, b_n) = \frac{P}{2\pi n} \frac{b_n}{a_n} \quad (6.1)$$

For the fitting approach, the offset current at the end of the pulse period was subtracted (baseline restoration) from each transient. Afterwards the following fitting function was applied to the transients:

$$I(t) = \frac{K}{\tau_e} \exp(-t/\tau_e), \quad (6.2)$$

where  $K$  is equal to  $\frac{gAW_{0nT}(0)}{2}$  according to Equation 3.10.

For a period of  $P = 8 \text{ ms}$  the first and second order sine and cosine coefficients are shown in Figure 6.5(a). The corresponding time constants for both methods are given in Figure 6.5(b). For temperatures above 250 K, they are in good accordance. For temperatures below 250 K, neither of the two approaches lead to correct time constants again due to the absence of transients at lower temperatures. Figure 6.5(c) and Figure 6.5(d) show Arrhenius plots and the extracted energies for the Fourier and the direct fitting approaches, respectively.

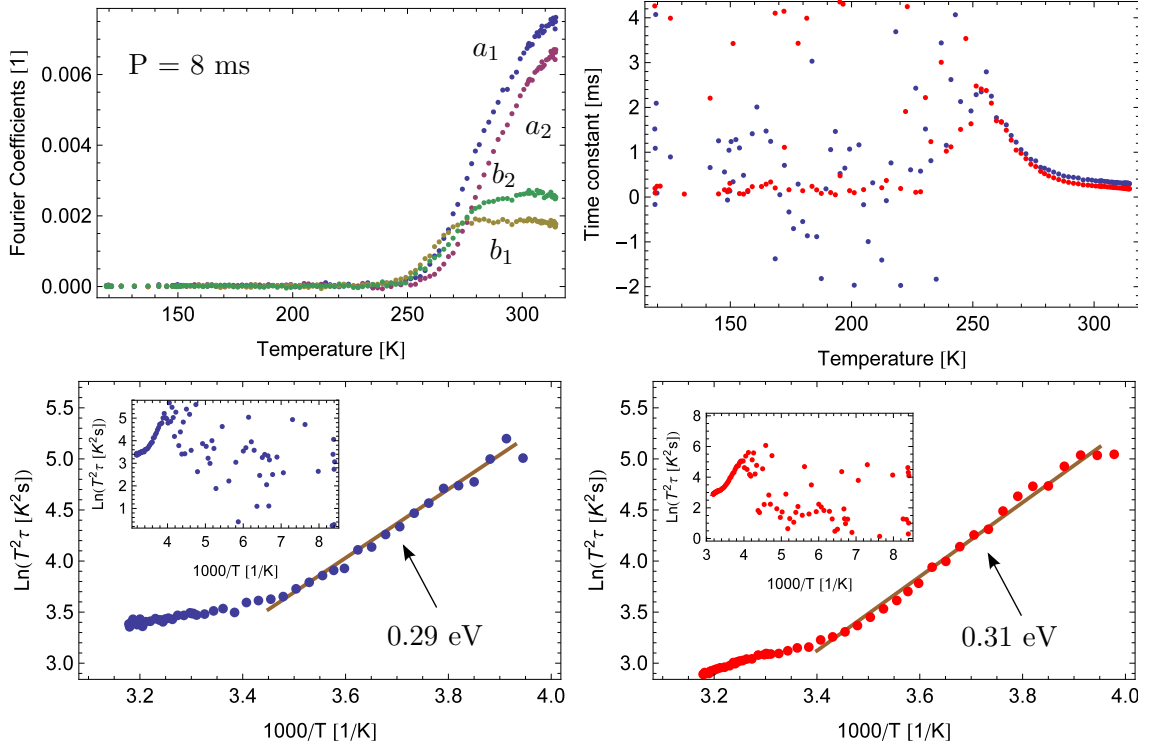


Figure 6.5: Results of Fourier and direct fitting approach. The first order Fourier coefficients are depicted in (a). The extracted time constants for the Fourier approach (blue) and direct fitting approach (red) are given in (b). The corresponding Arrhenius plots are shown in (c) and (d), respectively.

### 6.2.4 Carrier Trap Density

There are two ways to calculate the carrier trap density  $N_T$  from DLTS measurements. In the direct fitting approach, it is possible to obtain not only the time constant of the transients but also the pre-exponential factor  $K$  (see Equation 6.2), which can be used to determine the carrier trap density through  $n_T(0) = \frac{2K}{qAW_0}$ . We assume that at  $t = 0$  all traps are occupied by carriers, so that  $n_T(0)$  can be taken to be the total trap density  $N_T$ . This is shown for our data in Figure 6.6 in blue.

Alternatively, the trap density can also be obtained by integrating the area under the transient current curve according to the following equation:

$$n_{\text{int}} = \frac{Q}{e} = \frac{1}{e} \int_0^\infty I(t) dt = \frac{A}{e} \int_0^\infty J(t) dt, \quad (6.3)$$

where  $Q$  is the total amount of charge,  $e$  the electron charge and  $A$  the device area. This density is also indicated in Figure 6.6 in red, and is in good agreement with the direct fitting approach.

Furthermore, these carrier densities considered at room temperature are comparable to what was previously found with a Mott-Schottky (MS) analysis in Section 4.2.6. There, we found that the trap density  $N_T$  is in the order of  $2.5 \cdot 10^{16} \text{ cm}^{-3}$ .

From the trap density, we can calculate the number of traps per QD. The device area is given by  $0.0172 \text{ cm}^2$ . With a film thickness of 150 nm, the volume of the film is about

$2.5 \cdot 10^{-7} \text{ cm}^3$ . The QDs we use have a diameter of 3 nm and are separated by ligands with the length of 0.7 nm. By assuming a spherical volume of the QDs, the total number of QDs is approximately given as  $n_{\text{QDs}} = 7 \cdot 10^{12}$ . By multiplying the volume of the film with the trap density, the number of traps is determined to be  $n_{\text{traps}} = 6.3 \cdot 10^9$ . The number of traps per dots in the film is then given as:

$$\frac{n_{\text{traps}}}{n_{\text{QDs}}} = \frac{6.3 \cdot 10^9}{7 \cdot 10^{12}} \approx 10^{-3} \quad (6.4)$$

so that we conclude that in every thousand QDs there is one deep trap.

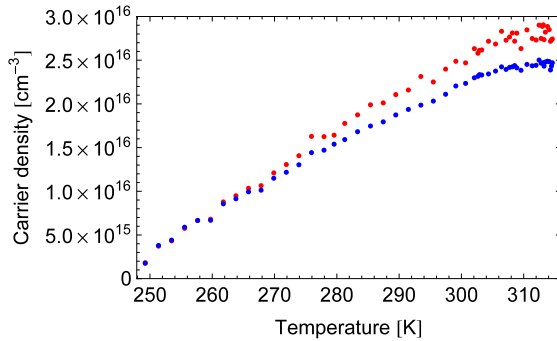


Figure 6.6: Carrier densities extracted from DLTS measurement with direct fitting approach (blue) and by integration of the transient area (red).

### 6.3 Temperature Dependent IV Curves and Concurrent DLTS Measurement

#### 6.3.1 Description of the Experiment

In a third experiment, IV curves were recorded with the ModuLab SMU in addition to DLTS data. In a first attempt, a BDT sample (A17S9) was cooled down from room temperature to 234 K while IV curves were recorded. In a successive warm-up phase from 241 to 338 K DLTS data were acquired from the same device. Data could not be recorded concurrently by then, since the pulsing signal from the DLTS set up disturbed the modulation signal from ModuLab and vice versa.

In a second attempt, IV and DLTS data were measured concurrently with an EDT sample (A17S7), while warming up the temperature from 246 to 337 K. This was achieved by turning off the pulse generator for 60 seconds after the temperature stabilisation was established at each measurement step. During this period, the IV curve and also the temperature was measured with the ModuLab SMU for a second device on the same sample (see Section 6.3.3).

### 6.3.2 DLTS Measurements

The measured emission transients are given for both samples in Figure 6.7. At both attempts, an instability of the current signal was observed when ramping the temperature below 242 K (blue curves in Figure 6.7(a) and (c)). The limit for high temperatures, however, was observed when temperature was ramped above 338 K (uppermost red curve in Figure 6.7(a)).

Between these temperature limits, transients could be observed and are depicted in Figure 6.7(b) and (d). For a DLTS measurement useful transients were found for the BDT sample only in a temperature range of 325 - 335 K and for the EDT sample in a range of 311 - 336 K, respectively. In each case, only five or six transients showed an exponential form.

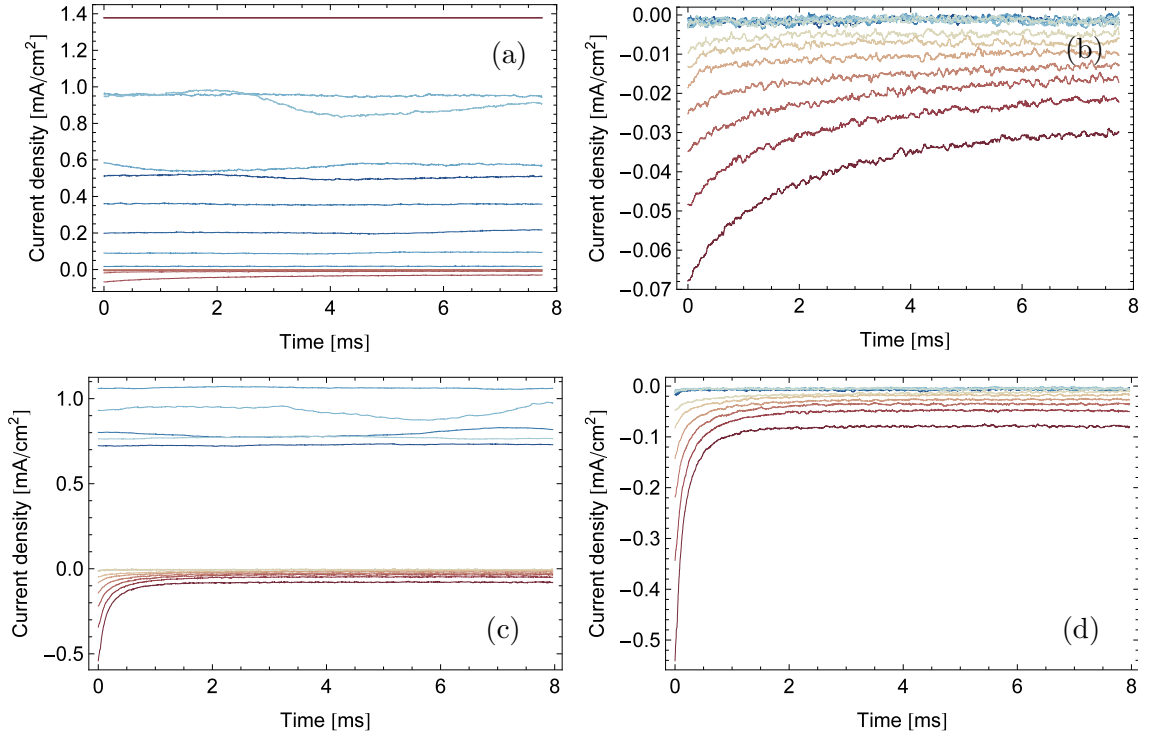


Figure 6.7: Temperature dependent current emission transients for second experiment. For sample A17S9 (BDT) and A17S7 (EDT), all measured signals - below, within and above the temperature limits of 242 K and 338 K - are shown in (a) and (c), respectively. In (b) and (d) only the transients within the valid temperature range are shown.

Figure 6.8 shows the flipped and restored transients for both samples. The small number of transients makes it difficult to perform a convincing DLTS analysis on both data sets. Nonetheless, the Fourier approach was used to analyse the two data sets. The Fourier coefficients and Arrhenius plots are given in Figure 6.9. For a fit to extract parameters, only five or six transients for the highest temperature are taken into consideration. For the BDT sample no clear region for such a fit could be found in the entire Arrhenius data, whereas for the EDT sample, a straight line was fitted giving an activation energy of 0.27 eV, which is comparable to the deep-level trap energies found in Section 6.2.

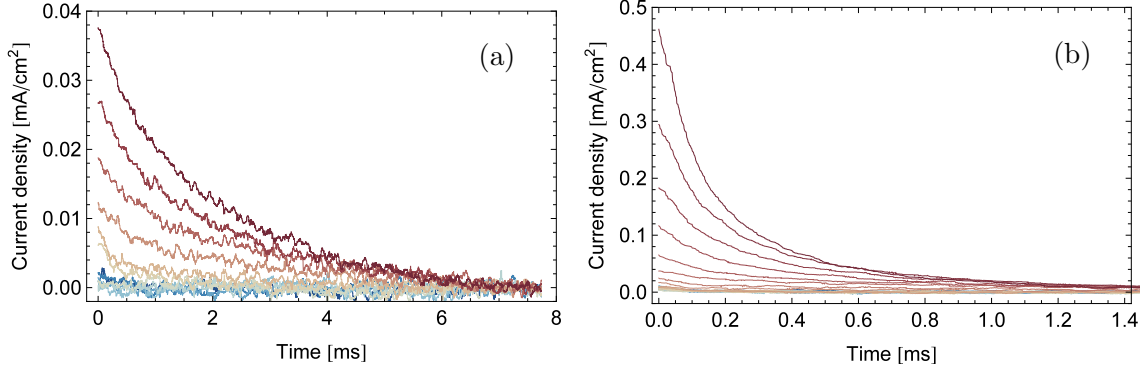


Figure 6.8: Flipped and baseline restored transients of Figure 6.7 are shown in (a) and (c) for sample A17S9 and A17S7, respectively.

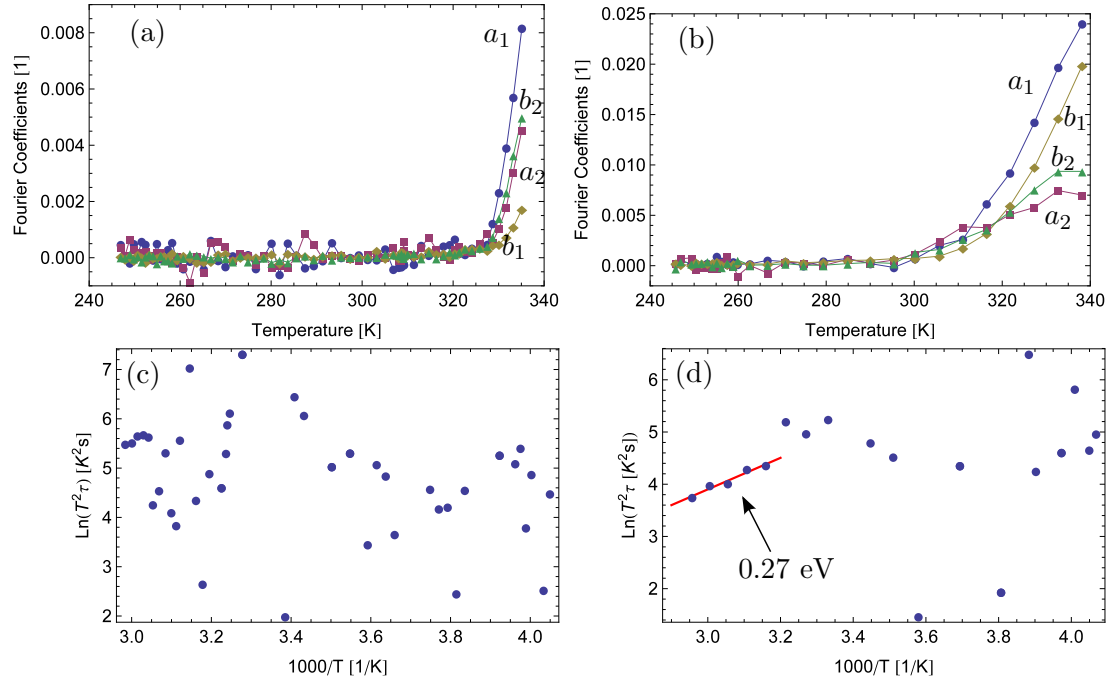


Figure 6.9: Fourier DLTS approach for second experiment. Fourier coefficients are given in (a) and (b) for sample A17S9 and A17S7, respectively. The corresponding Arrhenius plots are depicted in (c) and (d).

### 6.3.3 Temperature Dependent IV Measurements

To study the behaviour of the IV characteristic while changing the temperature, IV curves in the dark were recorded in parallel to the DLTS measurements. However, we observed that the measurement of temperature on the auxiliary channel perturbed the IV measurements using the *linear sweep impedance mode* (see Section 4.2.1). This difficulty could be circumvented by using the *linear sweep mode*, but this introduces other problems discussed below. Additionally, the scan rate was changed to a 30 mV/s, which was a trade-off between measurement duration and accuracy (or number of points).

Figure 6.10 depicts the measured raw data both linear and logarithmic, as well as the measurement direction. For both samples, a shift to lower values is observed when temperature is decreased. The same behaviour is also reported in Ref. [2]. Near the upper temperature limit (see Section 6.3.2), even the tail of the reverse bias shows a big temperature dependence as illustrated in Figure 6.10(c).

From the metrology point of view, several discontinuities occur, clearly visible in the logarithmic scale. They occur every time the ModuLab SMU changes its measurement range and was only observed for this mode, i.e. the linear sweep mode. For further investigations, the discontinuity around zero voltage was replaced with a linear curve fitted through points slightly above and below the discontinuity, whereas the rest was ignored.

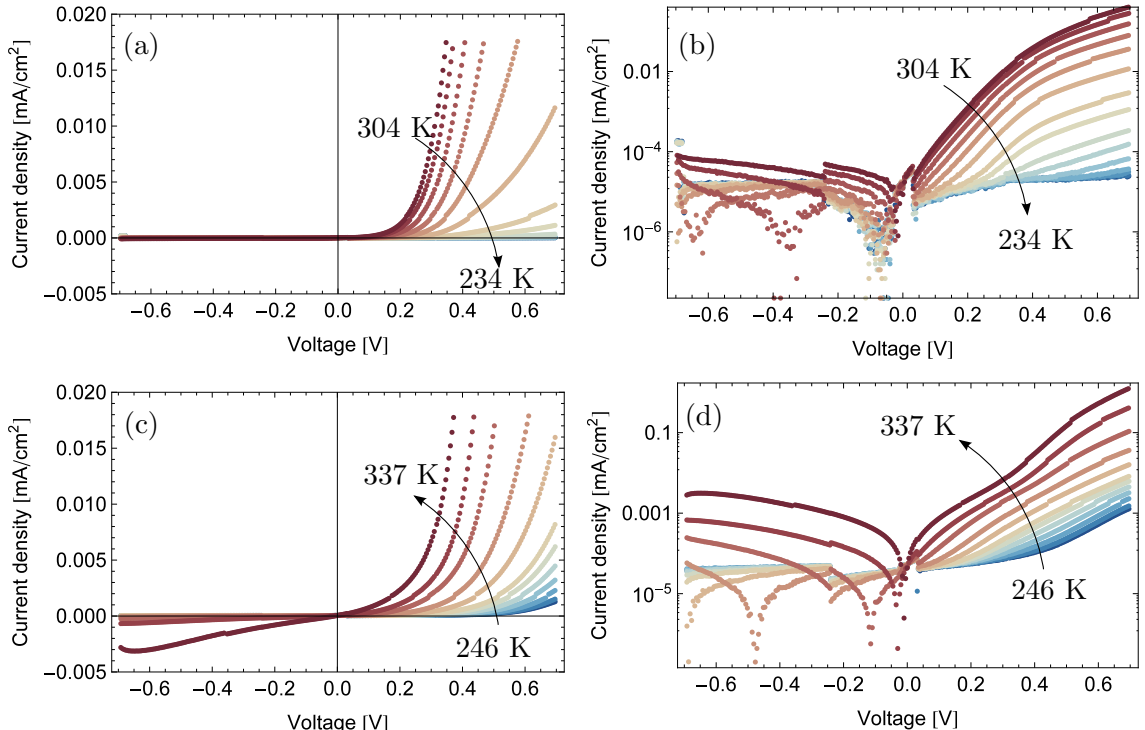


Figure 6.10: Temperature dependent IV characteristics. The IV curves for sample A17S9 are shown in linear and log scale in (a) and (b), whereas for sample A17S7 in (c) and (d), respectively. The temperature sweep direction is indicated with an arrow.

### 6.3.4 Saturation Current Model Fitting

The saturation current density  $J_s$  can be determined by fitting the exponential part of the IV (or JV) characteristic to the Shockley diode equation:

$$J = J_s \left( \exp\left(\frac{qV}{nkT}\right) - 1 \right), \quad (6.5)$$

where  $n$  is the ideality factor.

By fitting each of the measured IV curves as illustrated in Figure 6.11,  $J_s$  as a function of temperature was obtained. In the case of a Schottky diode, this dependence can be described by two common models:

- The thermionic emission model: Only carriers with an energy larger than the barrier height  $\phi_B$  can contribute to the current flow. The reverse current levels off and is given as:

$$J_s = A^* T^2 \exp\left(-\frac{q\phi_B}{kT}\right), \quad (6.6)$$

where  $A^*$  is the Richardson constant

$$A^* = 4\pi m^* k^2 / h^3. \quad (6.7)$$

- The diffusion model: The current flow is due to the difference in carrier concentrations and is limited by diffusion. The reverse current depends on the bias and is given as:

$$J_s = q\mu_p N_v \mathcal{E}_m \exp\left(-\frac{q\phi_B}{kT}\right), \quad (6.8)$$

where  $\mu_p$  is the hole mobility,  $N_v$  the effective density of states in valence band and  $\mathcal{E}_m$  the maximum electric field.

Both models were applied to the experimentally observed saturation currents  $J_s$  (see Figure 6.11(c) and (d)). Known or estimated material parameters used, are detailed in Appendix E. The diffusion model provided good agreement with  $J_s$ , whereas the thermionic emission model predicts smaller currents for lower temperatures. Especially for the EDT sample depicted in Figure 6.11(d), the difference is about one order of magnitude. Furthermore, the fitting process allowed extraction of the barrier height and is  $\phi_B = 0.67$  eV for the BDT sample and  $\phi_B = 0.58$  eV for the EDT sample, which is in good agreement with previously reported findings in Refs. [2, 12].

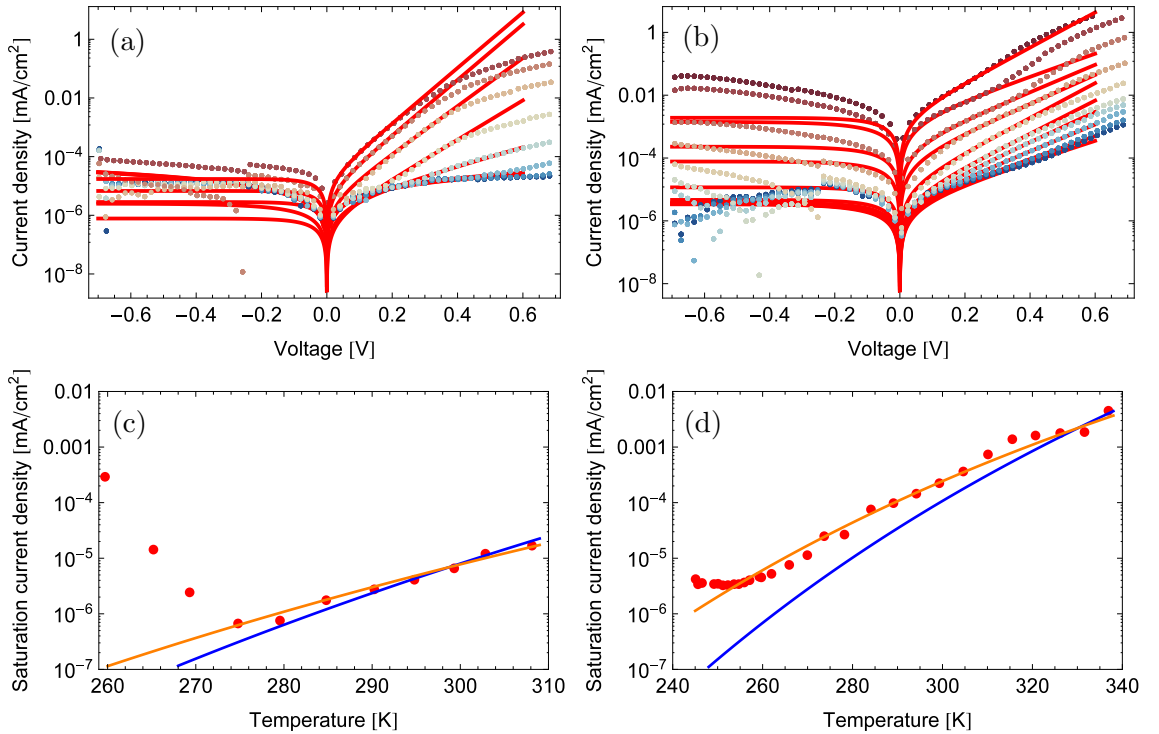


Figure 6.11: Temperature dependent IV characteristics of sample A17S9 (BDT) and A17S9 (EDT). The corresponding fits of Equation 6.5 are shown in (a) and (b), respectively. Extracted saturation current density and the two models (thermionic emission (blue), diffusion (orange)) are given in (c) and (d).

### 6.3.5 Summary and Conclusions

Three rounds of experiments were performed during this thesis to investigate traps in the fabricated PbS solar cells. In a initial experiment, the sample was cooled down and transients were searched with different measurement parameters, i.e. bias voltages and pulse widths. Transients were first observed when temperature was ramped toward room temperature. They show exponential decaying characteristic, where shortest time constant was measured to be 0.35 ms.

In the second experiment, transients were acquired and temperature was measured directly on the sample surface. From conventional and Gaussian boxcar approach an activation energy of 0.29 eV was extracted. For Fourier and direct fitting approaches, the extracted energies are 0.29 eV and 0.31 eV, respectively. The energies around 0.3 eV are not only comparable with respect to the approaches, but also to previous measurements on PbS colloidal QD photodetectors reported in Ref. [32]. From the same measurements, carrier trap density was estimated to be in the order of  $2.5 \cdot 10^{16} \text{ cm}^{-3}$ , which is in good agreement with observations from Mott-Schottky analyses presented in Section 4.2.6. Together with an estimation of the number of QDs in the film, the density was used to calculate the number of traps per QD. We found that one trap exists in every thousand QD.

In a final experiment, DLTS and temperature dependent IV measurements were performed. Temperature was varied within a range of 242 - 338 K, since the measured signal was unstable beyond these limits. To make a DLTS analyses on the data was difficult because only 5-6 transients with exponential decay could be observed. With the Fourier approach, 0.27 eV was extracted for the activation energy, which is comparable to the previous experiment. To the temperature dependent IV curves, two saturation current models were applied to experimentally extracted saturation currents (thermionic and diffusion model). The latter showed good agreement, with the experimentally extracted data. The extracted barrier heights are  $\phi_B = 0.67 \text{ eV}$  for the BDT sample and  $\phi_B = 0.58 \text{ eV}$  for the EDT sample, which is in good agreement with previously reported findings in Refs. [2, 12].

By considering the acquired energies, which lie all around 0.3 eV, we can conclude that we demonstrated the existence of deep-level traps (see Section 3.2). The emission spectrum of these QDs showed a first exciton peak at 950 nm, which corresponds to a band gap of 1.3 eV. Therefore, the traps states exists between the midgap and the band edge.



## Chapter 7

# Summary and Conclusion

This thesis presented deep-level transient spectroscopy (DLTS) as a powerful method to characterize deep-level traps in nanocrystal (NC) materials. For this purpose, all-inorganic conductive metal oxide/NC thin film/metal solar cells were fabricated. The active layer consists of a PbS NC film, which was deposited via layer-by-layer dip or spin coating.

A power conversion efficiency of 2.46% under AM1.5G conditions were obtained. Device degradation was investigated by measuring IV characteristics under dark and illumination over a period of seven days. In the dark, degradation stabilizes after 3-4 days. Under illumination, a drop of the short circuit current was observed, while the open circuit voltage stayed almost constant.

Impedance spectroscopy showed a CV dependences in the range from 0.1 Hz to about 500 Hz. For low frequencies and forward bias, Mott-Schottky analysis could be used to extract the carrier density about  $2.5 \cdot 10^{16} \text{ cm}^{-3}$  and built-in voltage between 0.12 V and 0.4 V. For reverse voltages and high frequencies, the model cannot be applied due to spatial and velocity limitations.

A DLTS setup was developed to investigate capacitance and current transients on the fabricated devices. For the purpose of automated data acquisition in the laboratory, two virtual devices were integrated in an existing LabVIEW framework. For the data processing, four DLTS algorithms were implemented in Mathematica.

DLTS measurements were successfully performed on PbS solar cells by investigating current transients. Capacitance transients could not be measured, because the fix measurement frequency of 1 MHz of the capacitance meter is too high to see a capacitance voltage dependence.

Analysis of the transients with the conventional Boxcar and Gaussian Boxcar gave a trap energy of 0.29 eV. With the Fourier and direct fitting approach comparable energies were extracted (0.29 eV and 0.31 eV). These energies indicate deep-level traps that lie between the mid gap and band edge, since the PbS cQD under investigation have a band gap of 1.3 eV.

A trap density of  $2.5 \cdot 10^{16} \text{ cm}^{-3}$  is extracted from the transients by integrating the area under the curves and also from the direct fitting approach and is in good agreement with the Mott-Schottky analysis. From the density and an estimation of the number of QDs in the film, we estimate that one trap exists in every thousand QD. This is compared to heavily doped silicon, since the atomic density of silicon is about  $5 \cdot 10^{22} \text{ cm}^{-3}$ .

DLTS and temperature dependent IV curves were recorded in a final experiment for a BDT and an EDT sample. An analysis of the DLTS data was difficult because only 5-6 transients could be observed. However, the Fourier approach applied on data of the BDT sample showed an activation energy of 0.27 eV, which is consistent with the other experiments. The IV curves showed a continuous shift toward lower current values when temperature is decreased. Furthermore, two models were used to fit the experimental extracted saturation current densities, namely thermionic emission and diffusion model. The former model predicts lower current densities at low temperatures, whereas the diffusion model provides good agreement with experimental data.

Finally, we note that by using relative fast time scales (i.e. transients in the ms range), we obtained meaningful data about trap densities within a total experimental time frame of 1-2 hours. This experimental window is short enough that we anticipate that we do not observe degradation of the device during our measurements.

In conclusion, this thesis shows that DLTS is a powerful technique to investigate and understand the origin of deep-level traps in nanocrystal materials.

# Chapter 8

## Outlook

This thesis showed the possibility of applying DLTS to colloidal solar cells with NC thin film active layers. Several areas for future work on using DLTS to understand the origin of traps are discussed in the following.

### Device properties

In this thesis, PbS cQD with EDT and BDT ligands were used. Recent work has shown the importance of surface treatments. DLTS measurements could be used to investigate whether a particle surface treatment affects deep trap states. This study should be also conducted as a function of NC layer thickness, and the DLTS results should be correlated to the actual device performance.

### Degradation effect

We observed that degradation occurs in our solar cells over a period of 7 days in ambient conditions. For example, in the second experiment, where a 3 week old sample was used, the temperature range over which the transients could be observed was much smaller and shifted towards higher temperatures. In future work, DLTS measurements could be systematically performed in air and in inert atmosphere over a period of several days. Device degradation may be related to the appearance of trap states and could thus be investigated using DLTS.

### Measurement time scales

In addition to temperature and voltage, times is a third parameter that could be adjusted while acquiring transients. In this thesis, DLTS measurements were performed in the millisecond time scale. Voltage pulses ranged from 0.1 ms to 10 ms and measurement period for the emission transients ranged from 1 ms to 100 ms. Future investigations could be done with shorter and longer time scales.

### Algorithms

A significant disadvantage of the conventional DLTS treated in this thesis is the poor energy resolution. Even a perfect trap produces a broad line in the DLTS spectrum, which can overlap with another trap. Laplace DLTS can provide an order of magnitude higher energy resolution and can separate states with very similar emission rates [23]. It gives the spectral density as a function of emission rate, by calculating the inverse Laplace transform of a transient. Due to the increased complexity of this analysis, Laplace DLTS was not within the scope of this thesis, but should be investigated in the future.



# Bibliography

- [1] A. Fafarman, K. W. B. Diroll, D. Kim, D. Ko, S. Oh, X. Y. and. Doan-Nguyen, M. Crump, and D. Reifsnnyder, “Thiocyanate capped nanocrystal colloids: A vibrational reporter of surface chemistry and a solution-based route to enhanced coupling in nanocrystal solids,” *Journal of the American Chemical Society*, vol. 133 (39), pp. 15 753–15 761, 2011.
- [2] K. Szendrei, “Charge extraction from colloidal inorganic nanocrystals,” Ph.D. dissertation, University of Groningen, The Netherlands, 2011.
- [3] J. Tang, X. Wang, L. Brozozowski, D. A. Barkhouse, R. Debnath, L. Levina, and E. Sargent, “Schottky quantum dot solar cells stable in air under solar illumination,” *Advanced Materials*, vol. 22, Issue 12, pp. 1398–1402, 2010.
- [4] N. Zhao, Doan-Nguyen, T. P. Osedach, X. Y. L.-Y. C. Doan-Nguyen, S. M. Geyer, D. Wanger, M. T. Binda, A. C. Arango, M. G. Bawendi, and V. Bulovic, “Colloidal pbs quantum dot solar cells with high fill factor,” *ACS Nano*, vol. 4 (7), pp. 3743–3752, 2010.
- [5] C. J. Brabec, S. Shaheen, C. Winder, S. Sariciftci, and D. Patrick, “Effect of lif/metal electrodes on the performance of plastic solar cells,” *Appl. Phys. Lett.*, vol. 80, 2002.
- [6] L. Hung, C. tand, and M. Mason, “Application of an ultrathin lif/al bilayer in organic surface-emitting diodes,” *Appl. Phys. Lett.*, vol. 78, 2001.
- [7] K. Choudhury, J. Yoon, and S. F., “Lif as an n-dopant in tris 8-hydroxyquinoline aluminum thin films,” *Advanced Materials*, vol. 20, pp. 1456 – 1461, 2008.
- [8] J. Luther, M. Law, M. Beard, Q. Song, M. Reese, R. Ellingson, and A. Nozik, “Schottky solar cells based on colloidal nanocrystal films,” *Nano Letters*, vol. Vol. 8, No. 10, pp. 3488–3492, 2008.
- [9] S. W. Tsang, H. Fu, R. Wang, J. Lu, K. Yu, and Y. Tao, “Highly efficient cross-linked pbs nanocrystal/c<sub>60</sub> hybrid heterojunction photovoltaic cells,” *Applied Physics Letters*, vol. 95, no. 18, p. 183505, 2009.
- [10] R. Debnath, J. Tang, D. A. Barkhouse, X. Wang, A. G. Pattantyus-Abraham, L. Brzozowski, L. Levina, and E. H. Sargent, “Ambient-processed colloidal quantum dot solar cells via individual pre-encapsulation of nanoparticles,” *Journal of the American Chemical Society*, vol. 132, no. 17, pp. 5952–5953, 2010.

- [11] S. Willis, C. Cheng, H. Assender, and A. Wat, “The transitional heterojunction behavior of pbs/zno colloidal quantum dot solar cells,” *Nano Letters*, vol. 12 (3), pp. 1522–1526, 2012.
- [12] J. Clifford, K. Johnston, L. Levina, and E. Sargent, “Schottky barriers to colloidal quantum dot films,” *Appl. Phys. Lett.*, vol. 91, 2007.
- [13] K. B.-A. Alexiev, Dimitri Scott, “Calculation of the response of a miller exponential signal correlator to odlts signals,” *Applied Physics*, vol. 4, pp. 1855–1856, 1993.
- [14] M. Bleicher, “Schottky-barrier capacitance measurements for deep level impurity determination,” vol. 16, pp. 375–380, 1973.
- [15] P. Blood and J. Orton, “The electrical characterisation of semiconductors,” *Rep. Prog. Phys.*, vol. 41, pp. 159–250, 1978.
- [16] J. A. Borsuk, “Current Transient Spectroscopy : A High-Sensitivity,” no. 12, pp. 2217–2225, 1980.
- [17] R. et al. Brunwin, “Detection of minority-carrier traps using transient spectroscopy,” *Electronics Letters*, pp. 2–3, 1979.
- [18] R. a. Bube, “Luminescence and trapping in zinc sulfide phosphors with and without copper activator,” *Physical Review*, vol. 80, pp. 655–666, 1955.
- [19] R. H. Bube, *Photoconductivity of Solids*, 1st ed. Wiley and Sons, 1960.
- [20] M. G. Buehler and T. Instruments, “Impurity centers in pn junctions determined from shifts in the thermally stimulated current and capacitance response with heating rate,” vol. 15, pp. 69–79, 1972.
- [21] A. Chantre, “Deep-level optical spectroscopy in GaAs,” *Phys. Rev. B.*, vol. 23, no. 10, 1981.
- [22] J. J. Choi, Y.-F. Lim, M. B. Santiago-Berrios, M. Oh, B.-R. Hyun, L. Sun, A. C. Bartnik, A. Goedhart, G. G. Malliaras, H. D. Abrunia, F. W. Wise, and T. Hanrath, “PbSe nanocrystal excitonic solar cells,” *Nano Letters*, vol. 9, no. 11, pp. 3749–3755, 2009, PMID: 19719095.
- [23] L. Dobaczewski, a. R. Peaker, and K. Bonde Nielsen, “Laplace-transform deep-level spectroscopy: The technique and its applications to the study of point defects in semiconductors,” *Journal of Applied Physics*, vol. 96, no. 9, p. 4689, 2004.
- [24] J. W. Farmer, “Charge transient spectroscopy,” *Applied Physics Letters*, vol. 41, no. 11, p. 1063, 1982.
- [25] M. A. Green, K. Emery, Y. Hishikawa, W. Warta, and E. D. Dunlop, “Solar cell efficiency tables (version 39),” *Progress in Photovoltaics: Research and Applications*, vol. 20, no. 1, pp. 12–20, 2012.
- [26] H. W. Hillhouse and M. C. Beard, “Solar cells from colloidal nanocrystals: Fundamentals, materials, devices, and economics,” *Current Opinion in Colloid & Interface Science*, vol. 14, no. 4, pp. 245 – 259, 2009.

- [27] K. Hoelzlein, G. Pensl, M. Schulz, and P. Stolz, "Fast computer-controlled deep level transient spectroscopy system for versatile applications in semiconductors," *Review of Scientific Instruments*, vol. 57, no. 7, p. 1373, 1986.
- [28] C. Hurtet, M. Boulou, a. Mitonneau, and D. Bois, "Deep-level spectroscopy in high-resistivity materials," *Applied Physics Letters*, vol. 32, no. 12, p. 821, 1978.
- [29] K. Ikeda and H. Takaoka, "Deep Level Fourier Spectroscopy for Determination of Deep Level Parameters," *Japanese Journal of Applied Physics*, vol. 21, no. 3, p. 462, 1981.
- [30] N. M. Johnson, D. J. Bartelink, R. B. Gold, and J. F. Gibbons, "Constant-capacitance DLTS measurement of defect-density profiles in semiconductors," *Journal of Applied Physics*, vol. 50, no. 7, p. 4828, 1979.
- [31] L. Kimerling, "New Developments in Defect Studies," *IEEE Transactions on Nuclear Science*, vol. 23, no. 6, 1976.
- [32] G. Konstantatos and E. Sargent, "Pbs colloidal quantum dot photoconductive photodetectors: Transport, traps, and gain," *Appl. Phys. Lett.*, vol. 91, 2007.
- [33] H. Kukimoto, C. Henry, and F. Merritt, "Photocapacitance studies of the oxygen donor in gap. i. optical cross sections, energy levels, and concentration," *Phys. Rev. B*7, vol. 7,6, pp. 2486–2499, 1973.
- [34] D. V. Lang, "Deep-level transient spectroscopy: A new method to characterize traps in semiconductors," *Journal of Applied Physics*, vol. 45, no. 7, p. 3023, 1974.
- [35] B. Lax, "Transient Response of a p-n Junction," *Journal of Applied Physics*, vol. 25, no. 9, p. 1148, 1954.
- [36] W. H. Lee and V. G. Cho, *Handbook of Sustainable Energy*. Nova Publishers, 2011.
- [37] H. Lefevre, M. Schulz, I. A. Festkrperphysik, and D. Freiburg, "Applied Physics Double Correlation Technique ( DDLTS ) for the Analysis of Deep Level Profiles in Semiconductors," *Applied Physics*, vol. 53, 1977.
- [38] D. L. Losee, "Admittance spectroscopy of impurity levels in Schottky barriers," *Journal of Applied Physics*, vol. 46, no. 5, p. 2204, 1975.
- [39] G. L. Miller, J. V. Ramirez, and D. a. H. Robinson, "A correlation method for semiconductor transient signal measurements," *Journal of Applied Physics*, vol. 46, no. 6, p. 2638, 1975.
- [40] A. G. Milnes, *Deep impurities in semiconductors*. Wiley, 1973.
- [41] H. Okushi and Y. Tokumaru, "Isothermal Capacitance Transient Spectroscopy for Determination of Deep Level Parameters," *Japanese Journal of Applied Physics*, vol. 19, no. 6, pp. 335–338, 1980.
- [42] J. A. Pals, "Properties of Au, Pt, Pd and Rh Levels in silicon measured with constant capacitance technique," *Solid-State Electronics*, vol. 17, pp. 1139–1145, 1974.

- [43] P. M. Petroff and D. V. Lang, "A new spectroscopic technique for imaging the spatial distribution of nonradiative defects in a scanning transmission electron microscope," *Applied Physics Letters*, vol. 31, no. 2, p. 60, 1977.
- [44] J. T. Randall and M. H. F. Wilkins, "Phosphorescence and Electron Traps. I. The Study of Trap Distributions," *Proceedings of the Royal Society A: Mathematical, Physical and Engineering Sciences*, vol. 184, no. 999, pp. 365–389, Nov. 1945.
- [45] A. Rohatgi, J. R. Davis, R. H. Hopkins, and P. G. McMullin, "A study of grown-in impurities in silicon by deep-level transient spectroscopy," *Solid-State Electronics*, vol. 26, no. II, pp. 1039–1051, 1983.
- [46] C. Sah, "Bulk and interface imperfections in semiconductors," *Solid-State Electronics*, vol. 19, pp. 975–990, 1973.
- [47] C. Sah, W. Chan, H. Fu, and J. Walker, "Thermally stimulated capacitance (tscap) in p-n junctions," *Appl. Phys. Lett.*, vol. 20, pp. 193–197, 1971.
- [48] C. Sah and L. Forbes, "Thermal and optical emission and capture rates and cross sections of electrons and holes at imperfection centers in semiconductors from photo and dark junction current and capacitance experiments," *Solid-State Electronics*, vol. 13, pp. 759–788, 1970.
- [49] E. H. Sargent, "Solar cells, photodetectors, and optical sources from infrared colloidal quantum dots," *Advanced Materials*, vol. 20, pp. 3958–3964, 2008.
- [50] D. K. Schroder, *Semiconductor Material and Device Characterisation*, 3rd ed., 2006.
- [51] S. Schulz, "Kapazitaets- und Kapazitaetstransientenspektroskopie an selbstorganisiert gewachsenen Dissertation zur Erlangung des Doktorgrades des Fachbereichs Physik der Universitaet Hamburg vorgelegt von Stephan Schulz aus Hamburg Hamburg," Ph.D. dissertation, Hamburg, 2005.
- [52] W. Shockley and H. J. Queisser, "Detailed balance limit of efficiency of p-n junction solar cells," *Journal of Applied Physics*, vol. 32, 3, pp. 510–519, 1961.
- [53] P. Stallinga, *Electrical characterisation of organic electronic material and devices*. Wiley and, 2009.
- [54] P. Stallinga, H. Gomes, H. Rost, A. Holmes, and M. Harrison, "Minority-carrier effects in poly-phenylenevinylene as studied by electrical characterization," *J. Appl. Phys.*, vol. 89, p. 1713, 2001.
- [55] S. Sze and K. N. Kwok, *Physics of semiconductor devices*. Wiley, 2007.
- [56] C. Szeles, "Positron-Anihilation Spectroscopy," *Encyclopedia of Applied Physics*., pp. 607–632, 1996.
- [57] D. Talapin and C. Murray, "PbSe nanocrystal solids for n- and p-channel thin film field-effect transistors," *Science*, vol. 310, pp. 86–89, 2005.

- [58] J. Tang, L. Brzozowski, D. A. R. Barkhouse, X. Wang, R. Debnath, R. Wolowiec, E. Palmiano, L. Levina, A. G. Pattantyus-Abraham, D. Jamakosmanovic, and E. H. Sargent, “Quantum dot photovoltaics in the extreme quantum confinement regime: The surface-chemical origins of exceptional air- and light-stability,” *ACS Nano*, vol. 4, no. 2, pp. 869–878, 2010, pMID: 20104859.
- [59] L. R. Weisberg, “A Technique for Trap Determinations in Low-Resistivity Semiconductors,” *Journal of Applied Physics*, vol. 39, no. 11, p. 5149, 1968.
- [60] S. Weiss and R. Kassing, “Deep Level Transient Fourier Spectroscopy (DLTFS): A technique for the analysis of deep level properties,” *Solid-State Electronics*, vol. 31, no. 12, pp. 1733–1742, Dec. 1988.
- [61] B. W. Wessels, “Determination of deep levels in Cu-doped GaP using transient-current spectroscopy,” *Journal of Applied Physics*, vol. 47, no. 3, p. 1131, 1976.
- [62] R. Williams, “Determination of Deep Centers in Conducting Gallium Arsenide,” *Journal of Applied Physics*, vol. 37, no. 9, p. 3411, 1966.
- [63] Y. Zohata, “A New Method for Determination of Deep-Level Impurity Centers in Semiconductors,” *Applied Physics Letters*, vol. 17, no. 7, p. 284, 1970.



## **Appendix A**

# **Database of Colloidal Solar Cells Fabricated for This Thesis**

Sample	QD Solution				Solvent	Linker solution	
	Name	Concentration	Quantity	Molecule		Molar	Quantity per block
A14S1	PbS061B	5mg/ml	20ml	EDT	Acetonitrile (anhyd)	0.05M	20ml
A15S1	PbS061B	5mg/ml	20ml	EDT	Acetonitrile (anhyd)	0.05M	20ml
A15S2	PbS061B	5mg/ml	20ml	EDT	Acetonitrile (anhyd)	0.05M	20ml
A16S1	PbS061B	5mg/ml	2ml	BDT	Acetonitrile (anhyd)	0.02M	41.5g BDT + 2.92ml Acetonitrile
A16S2	PbS061B	5mg/ml	2ml	BDT	Acetonitrile (anhyd)	0.02M	41.5g BDT + 2.92ml Acetonitrile
A16S3	PbS061B	5mg/ml	2ml	BDT	Acetonitrile (anhyd)	0.02M	41.5g BDT + 2.92ml Acetonitrile
A16S4	PbS061B	5mg/ml	2ml	BDT	Acetonitrile (anhyd)	0.02M	11.4g BDT + 4ml Acetonitrile
A16S5	PbS061B	5mg/ml	2ml	BDT	Acetonitrile (anhyd)	0.02M	11.4g BDT + 4ml Acetonitrile
A16S6	PbS061B	5mg/ml	2ml	BDT	Acetonitrile (anhyd)	0.002M	11.4g BDT + 4ml Acetonitrile
A16S7	PbS061B	5mg/ml	2ml	BDT	Acetonitrile (anhyd)	0.002M	11.4g BDT + 4ml Acetonitrile
A17S1	PbS061B	5mg/ml	2ml	Ammonium	Acetonitrile (anhyd)	0.130M	N/A
A17S2	PbS061B	5mg/ml	2ml	EDT	Acetonitrile (anhyd)	0.002M	8.39 ul/mg EDT in 1ml Acetonitrile*
A17S3	PbS061B	5mg/ml	2ml	BDT	Acetonitrile (anhyd)	0.002M	14.2mg/ml BDT in 1ml Acetonitrile*
A17S4	PbS061B	5mg/ml	2ml	EDT	Acetonitrile (anhyd)	0.002M	8.39 ul/mg EDT in 1ml Acetonitrile*
A17S5	PbS061B	5mg/ml	2ml	BDT	Acetonitrile (anhyd)	0.002M	14.2mg/ml BDT in 1ml Acetonitrile*
A17S6	PbS061B	5mg/ml	2ml	EDT	Acetonitrile (anhyd)	0.002M	8.39 ul/mg EDT in 1ml Acetonitrile*
A17S7	PbS061C	5mg/ml	2ml	EDT	Acetonitrile (anhyd)	0.002M	8.39 ul/mg EDT in 1ml Acetonitrile*
A17S8	PbS061C	5mg/ml	2ml	BDT	Acetonitrile (anhyd)	0.002M	14.2mg/ml BDT in 1ml Acetonitrile*
A17S9	PbS061C	5mg/ml	2ml	BDT	Acetonitrile (anhyd)	0.002M	14.2mg/ml BDT in 1ml Acetonitrile*

Table A.1: Database for colloidal solar cells (1), \* = 0.1M, afterwards diluted to 0.002M using 80ul BDT or EDT in 3920 ul Acetonitrile

<b>Sample</b>	<b>Coating</b>	<b>Environement</b>	<b>After treatment</b>	<b>Block x Cycles</b>
A14S1	Dipping	Air	N/A	6 x5
A15S1	Dipping	Air	Acetonitrile (20ml)+ Hexane (40ml)	1x30
A15S2	Dipping	Air	Acetonitrile (20ml)	6x5
A16S1	Spinning	Air	N/A	1x6
A16S2	Spinning	Air	N/A	1x5
A16S3	Spinning	Air	Bath in Acetonitrile (5-10ml)	1x10
A16S4	Spinning	Air	Bath in Acetonitrile (5-10ml)	1x20
A16S5	Spinning	Air	Bath in Acetonitrile (5-10ml)	1x12
A16S6	Spinning	Air	Bath in Acetonitrile (5-10ml)	1x12
A16S7	Spinning	Air	Bath in Acetonitrile (5-10ml)	1x32
A17S1	Spinning	Air	Bath in Acetonitrile (10ml)	1x20
A17S2	Spinning	Air	Bath in Acetonitrile (10ml)	1x32
A17S3	Spinning	Air	Bath in Acetonitrile (10ml)	1x15
A17S4	Spinning	Air	Bath in Acetonitrile (10ml)	1x15
A17S5	Spinning	Air	Bath in Acetonitrile (10ml)	1x15
A17S6	Spinning	Air	Bath in Acetonitrile (10ml)	1x15
A17S7	Spinning	Air	Bath in Acetonitrile (10ml)	1x10
A17S8	Spinning	Air	Bath in Acetonitrile (10ml)	1x15
A17S9	Spinning	Air	Bath in Acetonitrile (10ml)	1x10

Table A.2: Database for colloidal solar cells (2)

Sample	Solution changing	Specials
A14S1	Change EDT after each 5th cycle	N/A
A15S1	Change Acetonitrile + Hexane halfway through	N/A
A15S2	Change EDT after each 5th cycle	N/A
A16S1	N/A	2drops PbS per cycle, 10 drops BDT per cycle
A16S2	N/A	10 drops PbS per cycle, 10 drops BDT per cycle
A16S3	N/A	BDT bath(!), Short-time bath in Acetonitrile
A16S4	Change Acetonitrile after 10 layers	BDT bath(!), Short-time bath in Acetonitrile
A16S5	N/A	BDT bath(!), Short-time bath in Acetonitrile
A16S6	N/A	New BDT concentration used (!)
A16S7	Change Acetonitrile after 10 layers	N/A
A17S1	N/A	1min in ammonium bath
A17S2	N/A	N/A
A17S3	N/A	N/A
A17S4	N/A	N/A
A17S5	N/A	N/A
A17S6	N/A	N/A
A17S7	N/A	N/A
A17S8	N/A	N/A
A17S9	N/A	N/A

Table A.3: Database for colloidal solar cells (3)

## Appendix B

### Dip Coater

For automatic sample preparation a dip coater was developed together with Deniz Bozyigit and is shown in Figure B.1. An Arduino micro-controller controls the two motors for horizontal and vertical movements. For each movement, a command has to be sent (from LabVIEW) to the Arduino and was defined as follows:

M,pos0,pos1,pos2,pos3,pos4,E

with

pos0: 0 = motor, 1 = servo, 2 = wait

pos1: no of motor (1 or 2) or servo (8,9,10,11)

pos2: 0 = absolute, 1 = relative

pos3: no of steps

pos4: speed in us/step or wait time in ms

For example: M,0,1,1,100,10,E

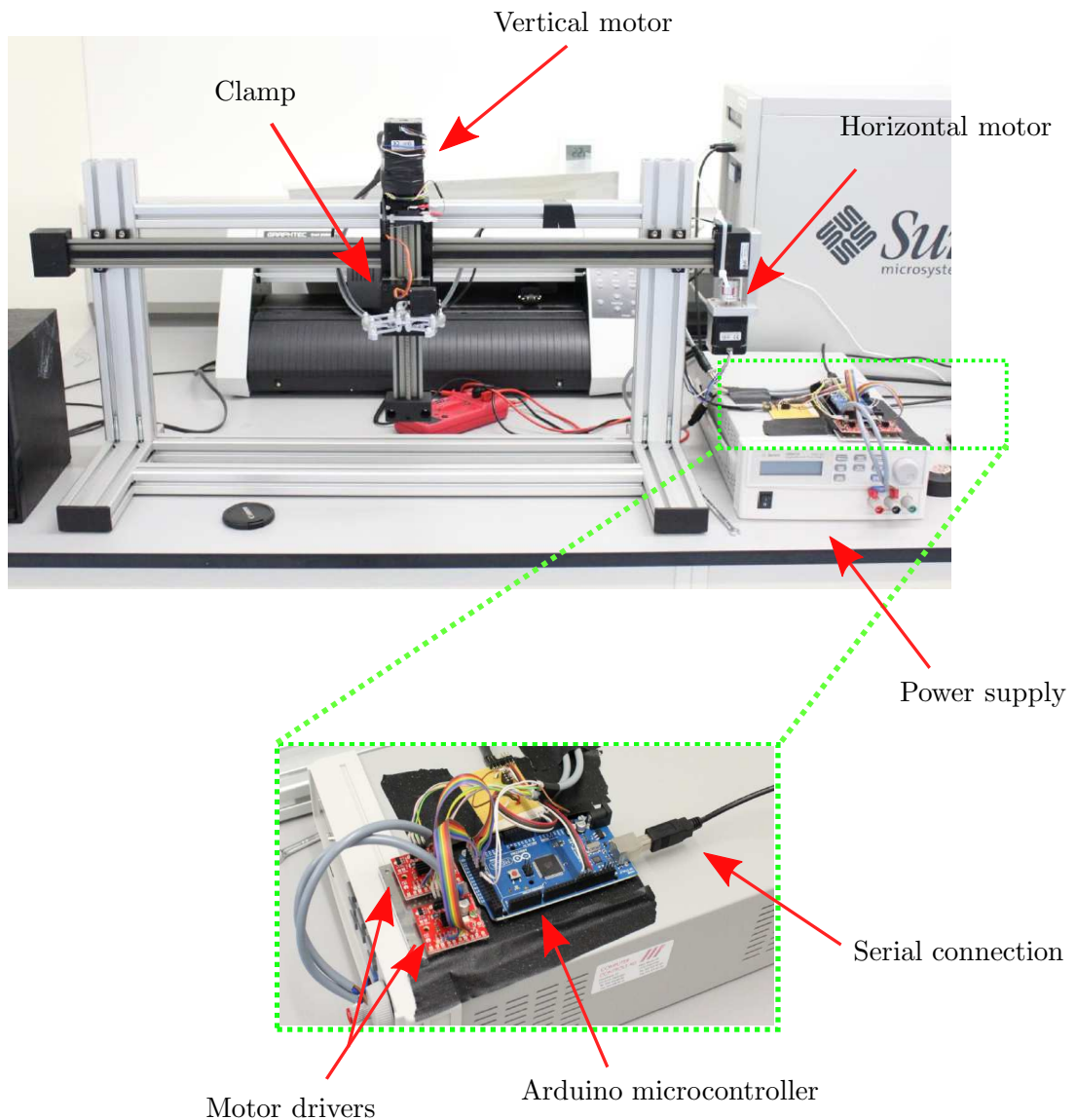


Figure B.1: Dip coater

## Appendix C

# Devices and Capacitance DLTS Setup

### C.1 Laboratory Devices

#### Pulse generator

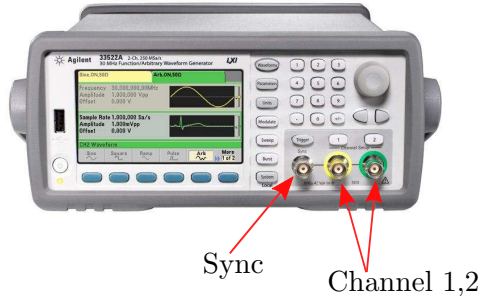


Figure C.1: Agilent 33522 Arbitrary Waveform Generator (AWG). Synchronize output and signal output are indicated.

Specification	Values
Output voltage	1 mVpp - 10 mVpp
Frequency	1 uHz – 30 MHz
Fall/Rise time	1 mVpp - 10 mVpp
Pulse width	16 ns, 100 ps resolution

Table C.1: Specifications of Agilent 33522 arbitrary waveform generator (AWG).

### Cryostat and temperature controller

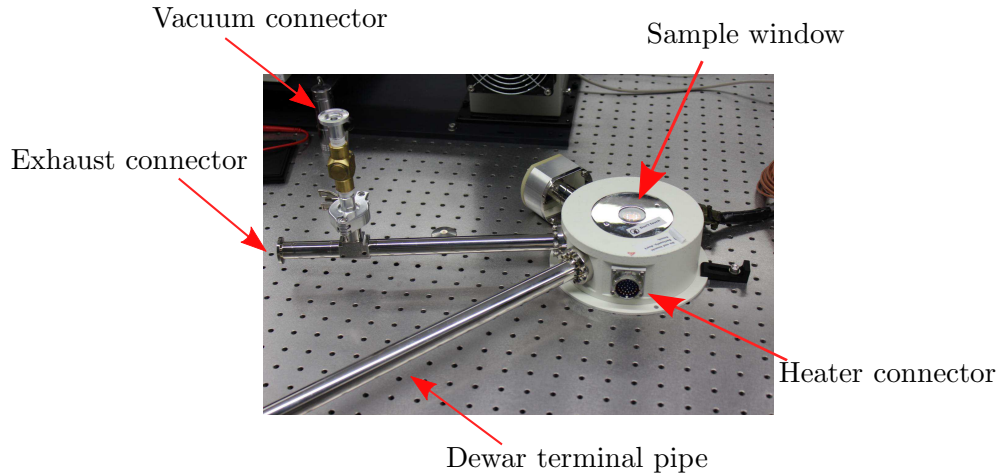


Figure C.2: Janis ST-500 cryostat. The connectors for dewar, heater, exhaust and vacuum pump are indicated.



Figure C.3: LakeShore 335 temperature controller.

Specification	Values
Range	3.5-475 K
Min. accuracy	1%
Max. variations	< 50 mK

Table C.2: Specifications of Janis ST-500 cryostat.

Specification	Values
Output channels	2
Temperature range	300 mK - 1505 K
Heating power	75 W
Heater ranges	Low, Medium, High
Setpoint ramping	0.1 - 100 K/min

Table C.3: Specifications of LakeShore 335 temperature controller.

### Capacitance bridge

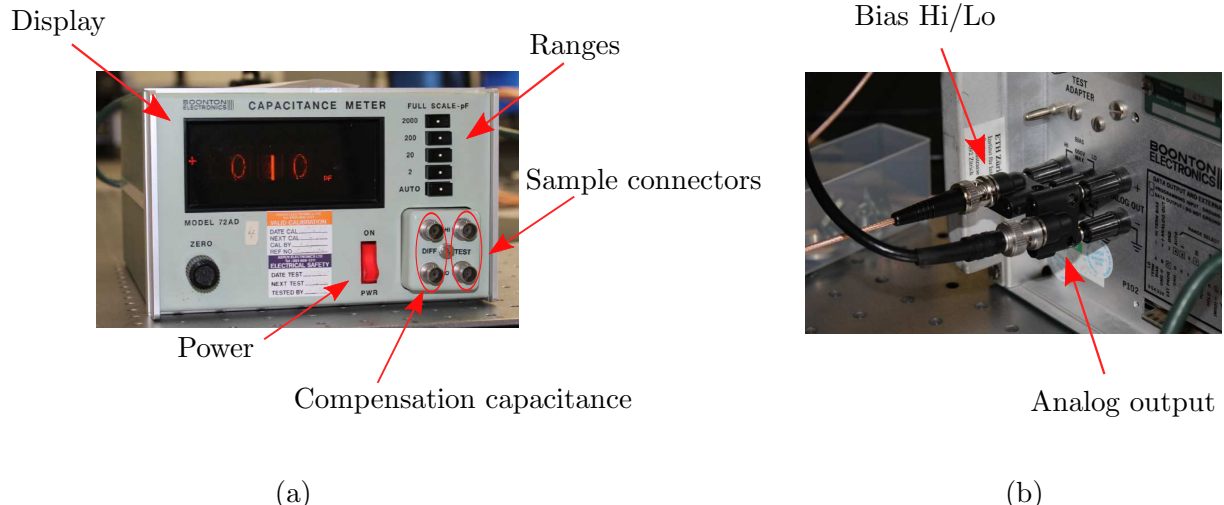


Figure C.4: Boonton 72ad capacitance meter. Front view is given in (a) and back view given in (b).

Specification	Values
Detection ranges	0.5 pF - 2000 pF
Resolution	0.001 pF
Input voltage	$\pm 600$ V
DC output voltage	$\pm 2$ V
Test frequency	1 MHz (fix)
Recovery time	50 $\mu$ m

Table C.4: Specifications of Boonton 72 capacitance meter.

### Transimpedance amplifier

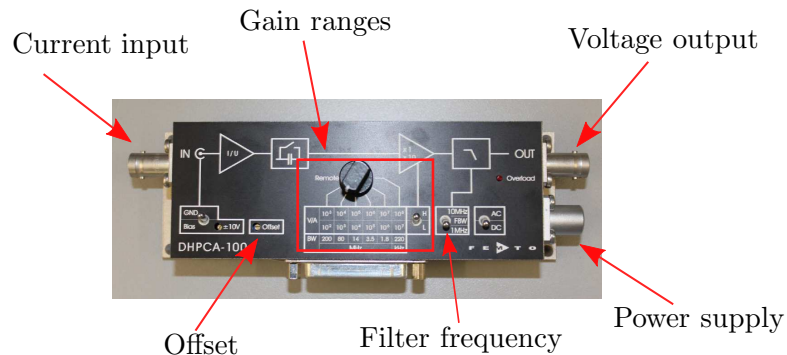


Figure C.5: Femto DHCPC transimpedance current amplifier.

Specification	Values
Transimpedance	$10^2 - 10^8 \text{ V/A}$
Bandwidth	< 200 MHz
Signal input voltage	$\pm 5 \text{ V}$
Slew rate	$1 \text{ V}/\mu\text{s}$
Output voltage range	$\pm 1 \text{ V}$

Table C.5: Specifications of Femto DHPCA transimpedance current amplifier.

### Oscilloscope



Figure C.6: Rohde and Schwartz RTM1054 oscilloscope

Specifications	Values
Number of channels	4
Bandwidth	500 MHz (at $50\Omega$ )
Resolution	8 bit
Max. sampling rate	2,5 Gsample/s

Table C.6: Specifications of Rohde and Schwartz RTM1054 oscilloscope.

## C.2 Capacitance and Current DLTS Setup

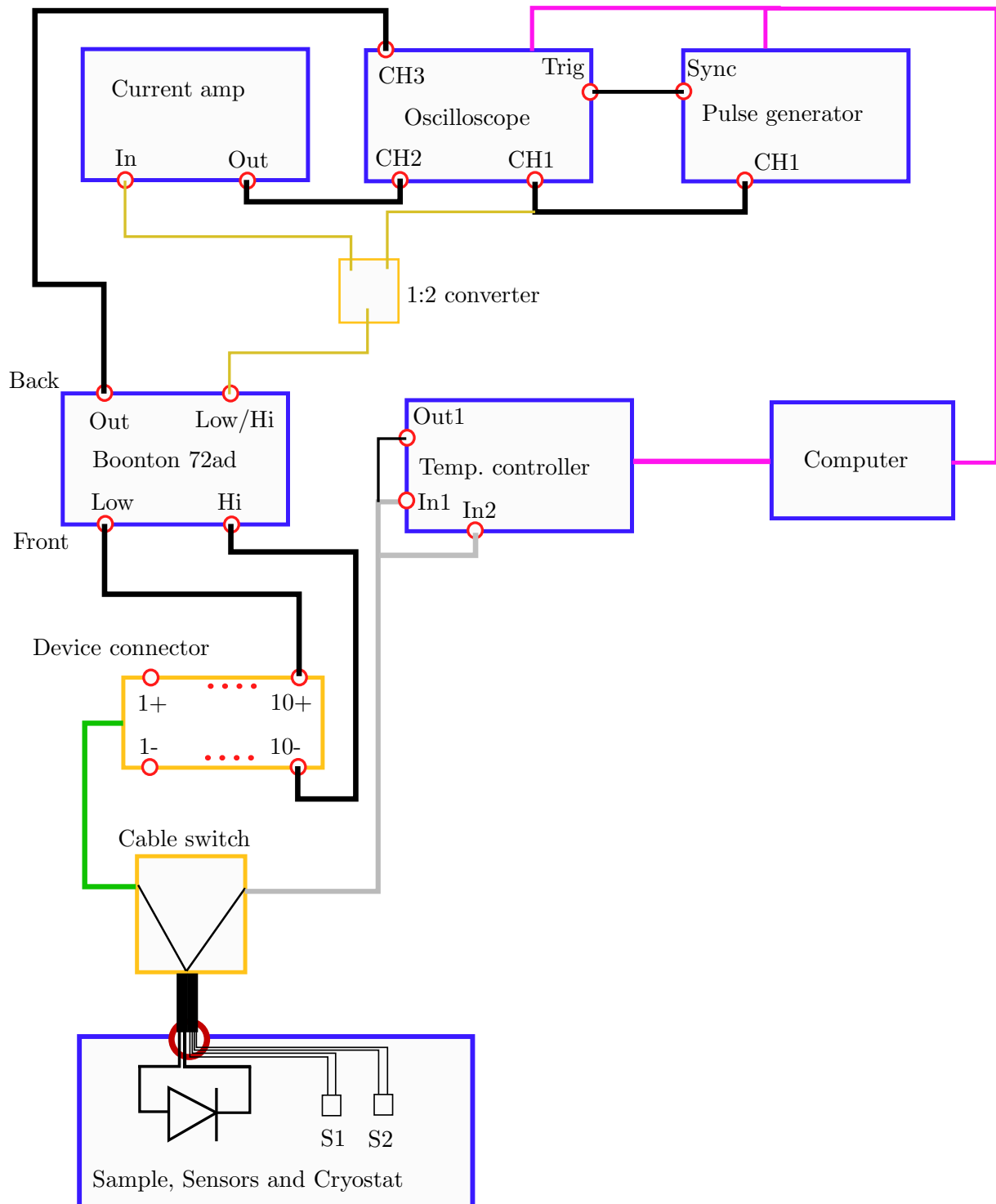


Figure C.7: Schematic of capacitance and current DLTS setup. The devices are depicted in blue and the cable connectors in yellow. Broad black lines indicate coax cables, pink lines represent USB-cables. Red circles signify connectors right at devices rack.

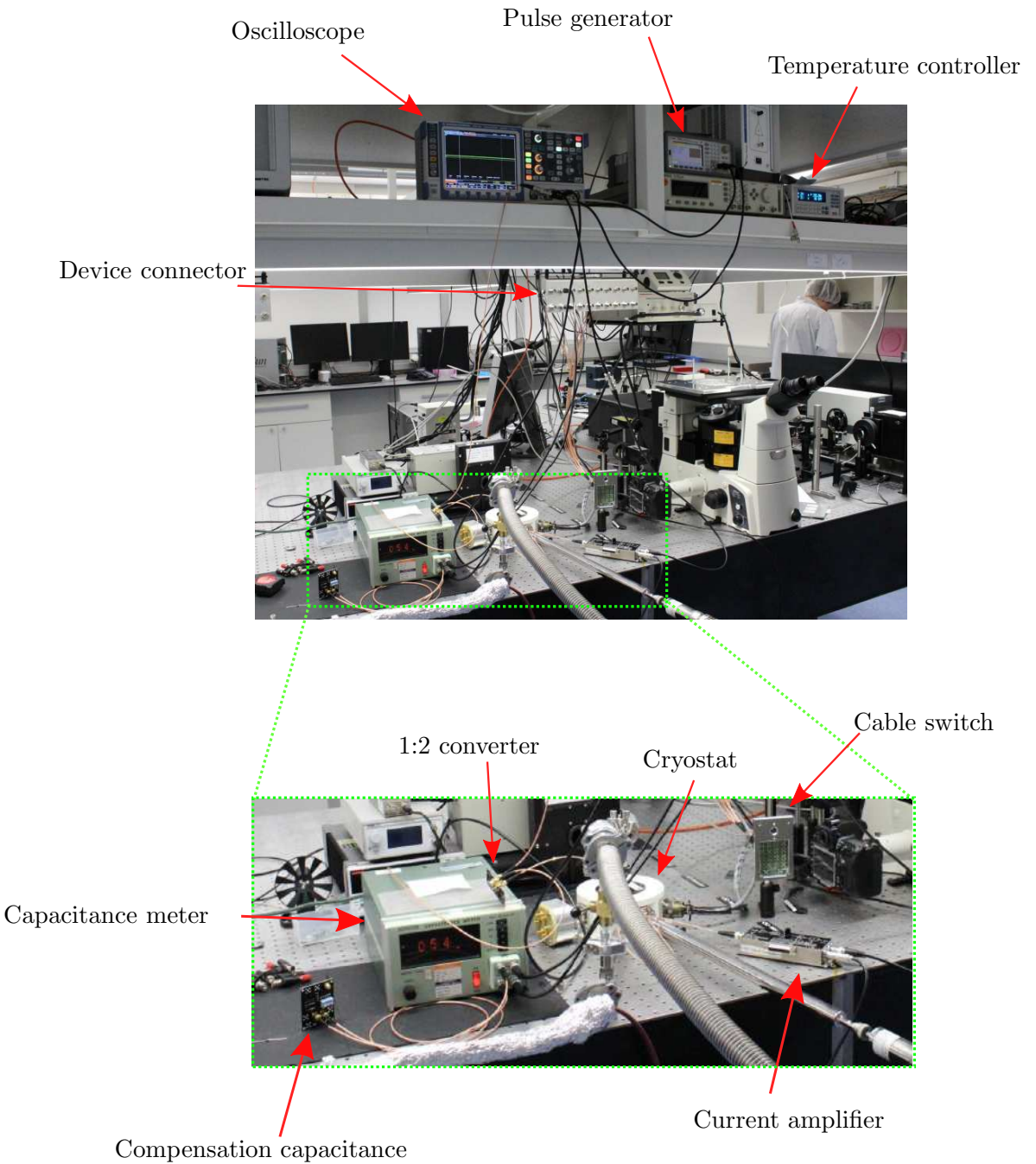


Figure C.8: Capacitance and current DLTS setup in laboratory. Oscilloscope, pulse generator and temperature controller are located on a ceiling table. The cryostat, current amplifier and capacitance meter are on the optical measurement table (green section). The dewar filled with liquid  $N_2$  and the vacuum pump stand on the floor (not shown).

## Appendix D

# LabVIEW Features

### D.1 Temperature and Voltage Sweep

Figure D.1 shows the interface for the virtual sweep instruments. The developed voltage and temperature sweep are added to this interface and can be chosen in the upper left. In the upper right the number of steps has to be set. The start and end voltages (baseline) are depicted in the lower left, whereas the start and end temperatures can be set in the lower right.

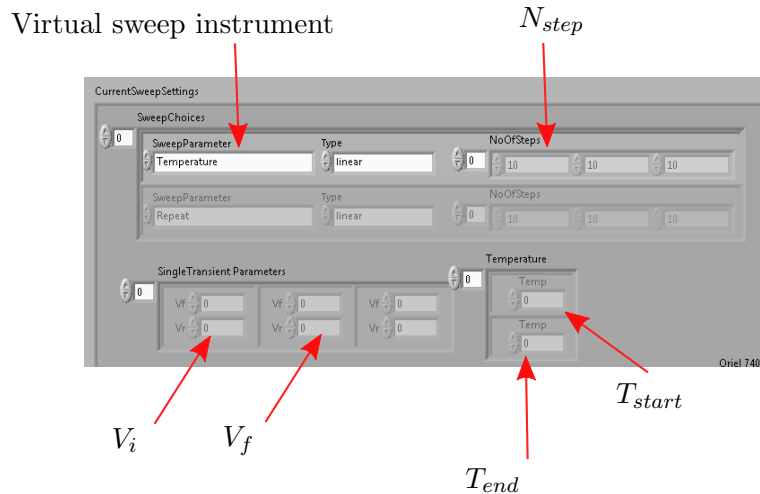


Figure D.1: LabVIEW sweep interface.

## D.2 Additional LabVIEW Settings

For a full functional measurement, settings additional to those explained in Section 5.3.1 has to be made. This addresses virtual instruments for the oscilloscope and the pulse generator. To the latter one belong two embedded virtual instruments, namely *PulseGen* and *Agilent33522*. The additional settings are summarized in Table D.2. The last three columns are fixed parameter settings, which can be applied by choosing one of the corresponding mode with the *Set other devices* button.

Additional LabVIEW settings		Single transient mode set. (fix)		
Virtual Instrument	Parameter name	Full	Moderate	Minimal
Oscilloscope	Trigger level	1 [V]	1 [V]	-
Oscilloscope	Trigger type	Edge	Edge	-
Oscilloscope	Channel	Ext	Ext	-
Oscilloscope	Ext. coupling	DC	DC	-
Oscilloscope	Waveform rate	Auto	Auto	Auto
Oscilloscope	Arithmetic	Average	Average	Average
Oscilloscope	Channels, Bandwidth	20 MHz*	-	-
Oscilloscope	Channels, Range	1.6**	-	-
Oscilloscope	Channels, Offset	0*	-	-
Oscilloscope	Channels, Acq. type	High resolution*	-	-
Oscilloscope	Channels, coupling	DC 1 MΩ*	-	-
PulseGen	Channel	CH1	CH1	-
PulseGen	Amplifier gain	No amp	No amp	-
PulseGen	RaiseTime	300 [ns]	300 [ns]	-
PulseGen	RaiseTime mode	absolut	absolut	-
PulseGen	Rep. polarity	0	0	-
PulseGen	NoOfPoints	5000	5000	-
PulseGen	CyclicShift	0	0	-
Agilent33522	Trigger mode	Internal	Internal	-
Agilent33522	Rate	40000 [Sa/s]	40000 [Sa/s]	-
Agilent33522	Sync mode	CH1	CH1	-
Agilent33522	Load (CH1)	10kΩ	10kΩ	-

Table D.1: Additional LabVIEW settings. Fix values are in the last three columns and set by single transient instrument. \* = holds for all four channels. \*\* = For all channels, except for channel 2 (0.8).

## Appendix E

# Saturation Current Models

All following formulas for the saturation current diffusion model are taken from [55].

According to thermionic emission theory the current density of a Schottky diode is given as

$$J = A^* T^2 \exp\left(-\frac{q\phi_B}{kT}\right) \left[\exp\left(\frac{qV}{kT}\right) - 1\right], \quad (\text{E.1})$$

where  $A^* = 4\pi m^* k^2/h^3$  is the Richardson constant,  $T$  the temperature,  $q$  the electron charge,  $\phi_B$  the Schottky barrier height,  $k$  the Boltzmann constant and  $V$  the applied voltage.

The saturation current density is therefore given as

$$J_s = A^* T^2 \exp\left(-\frac{q\phi_B}{kT}\right). \quad (\text{E.2})$$

For the fitting performed in this thesis, the Richardson constant was calculated to be  $A^* = 33648.6 \text{ mA/cm}^2/\text{K}^2$  by assuming that  $m^* = 0.2m_{\text{electron}}$ .

According to the diffusion theory the current density is given as

$$J = q\mu_p N_v \mathcal{E}_m \exp\left(-\frac{q\phi_B}{kT}\right) \left[\exp\left(\frac{qV}{kT}\right) - 1\right], \quad (\text{E.3})$$

where  $\mu_p$  is the hole mobility,  $N_v$  the effective density of states in valence band and  $\mathcal{E}_m$  the maximum electric field.

The saturation current density is therefore given as

$$J_s = q\mu_p N_v \mathcal{E}_m \exp\left(-\frac{q\phi_B}{kT}\right). \quad (\text{E.4})$$

For the fitting, the pre-exponential parameters were determined as follows:

- The hole mobility was taken from [2] as  $\mu_p = 4 \cdot 10^{-2} \text{ cm}^2/(\text{Vs})$
- The effective density of states was calculated from the following formula:  
 $N_v = 2(2\pi m^* kT/h^2)^{3/2} = 2.26379 \cdot 10^{18} \text{ cm}^{-3}/\text{K}^{3/2}\text{T}^{3/2}$  by assuming that  $m^* = 0.2m_{\text{electron}}$ .
- The maximum electric field was calculated with the following formula:  
 $\mathcal{E}_m = qN_D W_D/\epsilon = 0.113095 \text{ MV/cm}$ , where we took  $N_D = 5 \cdot 10^{16} \text{ cm}^{-3}$ ,  $\epsilon = 12\epsilon_{\text{vacuum}}$  and  $W_D = 150 \text{ nm}$  for the doping density, permittivity and depletion width, respectively.